Geothermal Energy

https://doi.org/10.1186/s40517-026-00375-8

Article in Press

Groundwater and geothermal archetypes in Berlin, Germany

Received: 22 Sep 2025

Accepted: 27 Jan 2026

Published online: 14 February 2026

Cite this article as: Javaran, M., Kreitmair, M., Makasis, N. *et al.* Groundwater and geothermal archetypes in Berlin, Germany. *Geotherm Energy* (2026). https://doi.org/10.1186/s40517-026-00375-8

Mohammad Javaran, Monika Kreitmair, Nikolas Makasis, Philipp Blum & Kathrin Menberg

We are providing an unedited version of this manuscript to give early access to its findings. Before final publication, the manuscript will undergo further editing. Please note there may be errors present which affect the content, and all legal disclaimers apply.

If this paper is publishing under a Transparent Peer Review model then Peer Review reports will publish with the final article.

ARTICLE IN PRESS

©The Author(s) 2026. **Open Access** This article is licensed under a Creative Commons Attribution 4.0 International License, which permits use, sharing, adaptation, distribution and reproduction in any medium or format, as long as you give appropriate credit to the original author(s) and the source, provide a link to the Creative Commons licence, and indicate if changes were made. The images or other third party material in this article are included in the article's Creative Commons licence, unless indicated otherwise in a credit line to the material. If material is not included in the article's Creative Commons licence and your intended use is not permitted by statutory regulation or exceeds the permitted use, you will need to obtain permission directly from the copyright holder. To view a copy of this licence, visit http://creativecommons.org/licenses/by/4.0/

Manuscript to be submitted to Geothermal Energy

Groundwater and geothermal archetypes in Berlin, Germany

Mohammad Reza Hajizadeh Javaran[a,*], Monika J. Kreitmair[b], Nikolas Makasis[b], Philipp Blum[a], Kathrin Menberg[a]

[a] Karlsruhe Institute of Technology (KIT), Institute of Applied Geosciences (AGW), Karlsruhe, Germany
[b] School of Engineering, University of Surrey, Guildford, United Kingdom

*Corresponding author: Mohammad Reza Hajizadeh Javaran, Email: mohammad.javaran@kit.edu

Keywords

subsurface urban heat islands, groundwater flow and heat transport, subsurface management, geothermal energy, urban groundwater

Abstract

Urban aquifers are influenced by several natural and anthropogenic factors, such as geological and hydrogeological conditions and built infrastructure, like heated basements, underground car parks, and train tunnels. Realistic 3D city-scale physics-based models of complex and heterogeneous aquifers must balance accuracy and efficiency to support scenario-based subsurface management. Hence, this study aims to provide an overview of the 3D thermal state of the urban subsurface of Berlin, Germany, with the goal of identifying groundwater and geothermal archetypes. Based on a detailed 3D geological model, covering an area of 118 km^2 and a depth of 250 m, block-divided (500 m × 500 m × 50 m), steady-state groundwater flow and heat transport models are created. These block models serve as a basis for identifying groundwater archetypes representing areas with similar hydrogeological and infrastructure conditions. The simulated, large-scale groundwater temperature patterns are generally in good agreement with interpolated temperatures from depth-oriented measurements. In addition, block-scale models capture thermal hot spots and low spots that are not detected by interpolated maps. Using regression-based decision trees, 38 groundwater archetypes are identified for the shallow anthropogenically influenced layer of blocks and 21 archetypes at deeper layers (> 50 m bgl).

Heated basements and groundwater head difference are the most contributing features in differentiating archetypes for the shallow layer of the blocks, while lower temperature boundary dominates selection of archetypes in deeper layers. Similarity of large-scale groundwater temperature patterns across different numbers of selected archetypes shows the robustness of the approach. Using thermal and geological criteria, 10 of the identified archetypes are classified as geothermal archetypes that indicate suitable conditions for ground source heat pump systems. The archetypes approach could be further developed to support other groundwater and subsurface uses, e.g., by considering groundwater-dependent ecosystems, legal aspects (e.g., groundwater contamination), and the interactions between different uses.

1. Introduction

The thermal state of the urban underground has gained substantial attention in recent decades due to its significance for subsurface thermal and hydraulic use (Attard et al., 2016; Epting et al., 2020; Tissen et al., 2021), underground ecosystem preservation (Becher et al., 2022), and sustainable urban planning (Ngarambe et al., 2025; Kho et al., 2025). The urban subsurface is affected by numerous anthropogenic activities, resulting in increased underground and groundwater temperatures (GWT), commonly known as the subsurface urban heat island (SUHI). SUHI has been extensively studied in many urban areas, like in Winnipeg, Canada (Ferguson & Woodbury, 2007), Osaka, Japan (Taniguchi et al., 2009), Moscow, Russia (Lokoshchenko & Korneva, 2015), Turin, Italy (Barla et al., 2018), Basel, Switzerland (Epting & Huggenberger, 2013), and six German cities (Menberg et al., 2013), highlighting the different anthropogenic and natural factors contributing to thermal anomalies in the subsurface. Among these factors are human-built drivers like underground car parks (Noethen et al., 2023), building basements and train tunnels (Loria et al., 2022), building and surface sealing (Alberto & Crosta, 2021), land surface sealing (Benz et al., 2015), as well as natural factors such as depth to groundwater (Böttcher & Zosseder, 2022), upstream groundwater flow (Zhu et al., 2015), surface water (Garcia

Gil et al., 2014), and subsurface properties such as heat capacity and porosity (Kreitmair et al., 2023).

A holistic view of the thermal state of the underground is crucial for effective management and sustainable thermal use of the subsurface (Blum et al., 2021). For example, mapping groundwater temperature by integrating field measurements, analytical heat transport solutions, and numerical groundwater modeling can promote utilization of ground source heat pumps (GSHP) and groundwater heat pumps (GWHP) by identifying areas with increased low-temperature geothermal potential (Garcia Gil et al., 2015). Using GWT data from measurements in the city of Vienna, key locations for open and closed loop systems could be identified (Tissen et al., 2021). In addition, city-scale numerical flow and heat transport models can help to assess the technologically achievable energy potential for reasonable exploitation of subsurface resources (Zhu et al., 2015; Epting et al., 2020).

GWT also has profound implications for drinking water quality, as it is a critical parameter influencing water quality (WHO, 2011; Benz et al., 2024). Furthermore, anthropogenic activities are stressors for groundwater ecosystems, especially invertebrate groundwater fauna (Koch et al., 2024). Groundwater ecosystems, particularly in shallow aquifers, can be affected by elevated GWT (Brielmann et al., 2011; Issartel et al., 2005). Hence, GWT mapping facilitates better ecosystem preservation (Becher et al., 2022; Koch et al., 2020; Noethen et al., 2024; Koch, 2024).

To address these diverse aspects of groundwater management, previous studies employed a range of predictive modeling approaches, including analytical, data-driven, and numerical approaches. Analytical approaches are used, for example, for assessing the shallow geothermal assessment of the German state of Baden-Württemberg (Ohmer et al., 2022), using existing datasets on heat extraction rates, surface temperature, and terrestrial heat flow, to determine the ability of the ground to meet building heating demand on a regional scale (Miocic & Krecher, 2022). The employed analytical approach to estimate the technical geothermal potential used *g*-functions (Eskilson, 1987) to optimize the heat extraction rates for the borehole heat exchangers (BHE).

Moreover, analytical approaches have been utilized to quantify and spatially map vertical anthropogenic heat fluxes from various surface sources through the unsaturated zone into the groundwater (Menberg et al., 2013; Benz et al., 2015). Despite showing promising results, analytical solutions are often too simplified and unable to capture local variations caused by different anthropogenic factors (Mueller et al., 2018).

Data-driven and machine learning-based methods have gained popularity in recent years due to their ability to process large datasets, for example, for mapping groundwater temperature for geothermal applications. For instance, neural networks were used to estimate groundwater temperature at different depths, enhancing the geothermal assessment accuracy in Cyprus (Kalogirou et al., 2012). Furthermore, machine learning techniques were applied to generate high-resolution 2D maps of shallow geothermal potential in Switzerland (Assouline et al., 2019). Although data-driven methods offer computational efficiency and broad applicability, they extensively rely on data as a prerequisite and often fail to capture the physics of the problem, reducing their wider applicability (Pelzer et al., 2025).

3D geological and hydrogeological models are widely used as tools across different subsurface applications, including groundwater flow and heat transport (Alcanié et al., 2021), engineering geology (Wu, 2005) and urban and environmental applications (Ciampi et al., 2024). They can support subsurface infrastructure planning and risk assessment by providing volumetric representation of subsurface and spatial continuity, which is not feasible with 2D geological cross sections or isolated boreholes (Wu 2005). Also, 3D geological models have been applied to address environmental and urban issues, such as guiding the identification of contamination sources, delineating contamination plumes, and providing remediation strategies for a complex subsurface setting (Ciampi et al., 2024). With respect to the simulation of groundwater flow and heat transport, 3D models are widely used as tools to analyze regional groundwater flow patterns and resulting temperature distributions for deep geothermal explorations on a basin scale (Alcanié et al., 2021). Building on such 3D geological models, previous studies also applied different numerical modeling approaches to investigate the groundwater thermal state in urban environments. However, in terms of exploring the impact of different factors on GWT distribution, numerical studies tend to focus on individual or a very limited number of factors. For example, a groundwater flow and heat transport model of the Leibnitzer Feld aquifer in Austria incorporated different land surface and climate inputs to optimize the thermal use of the shallow subsurface (Rock & Kupfersberger, 2018). Another 3D flow and heat transport model was developed to understand the thermally affected zones by both urban underground structures and geothermal systems (Attard et al., 2016).

However, using numerical city-scale thermo-hydraulic modeling of the subsurface for management purposes is computationally expensive, especially in terms of sensitivity analysis, calibration, validation, and analyzing different usage scenarios. Thus, some previous studies utilized scalable numerical modeling as a tool for thermal management of groundwater with simplified assumptions. Box model approaches are a computationally efficient and alternative framework to full-scale 3D flow and heat transport simulations. They have been used, for example, to assess the technical potential of low-temperature aquifer thermal energy storage (ATES) systems by developing homogeneous hydrogeological box models and modeling representative ATES configurations (Stemmle et al., 2024). Another city-scale modelling approach introduced an archetype-based framework to estimate subsurface thermal states efficiently across large urban areas. By clustering regions with similar hydrogeological state and thermal behaviour, and using a simplified layered geology, a computationally efficient mapping of thermal states of subsurface was generated (Kreitmair et al., 2023).

The objective of this study is to determine the 3D subsurface thermal state in a complex urban setting with heterogeneous hydrogeological conditions using an archetype approach and showcase the applicability of the approach for subsurface management. Hence, a detailed 3D geological model as well as block-scale numerical groundwater flow and heat transport models are developed to infer GWT across the modelling domain of city center of Berlin, Germany. This simulated thermal state, in combination with hydrogeological (e.g., depth to groundwater level, thermal conductivity) and built infrastructure features (e.g., basements, underground car parks, train tunnels), serves as a basis for the archetype identification via regression tree analysis. The robustness of the archetype approach is assessed through multiple regression analyses, based on different error thresholds, and the results are compared to interpolated GWT maps derived from groundwater measurements. Finally, to showcase the applicability of the groundwater archetypes for subsurface planning, these are classified further into geothermal archetypes to determine suitable locations (i.e., blocks) for closed GSHP systems.

2. Materials and methods

The workflow in this study comprises six steps, briefly outlined below and illustrated in Figure 1, with a detailed explanation given in subsequent sections.

1) The study area in the city center of Berlin, Germany, is delineated.
2) Using available data, such as geological cross sections, a 3D geological model is built. The model is then parametrized using available hydrogeological and anthropogenic infrastructure data.
3) The modeling area is divided into equally sized blocks (500 m × 500 m × 50 m), and groundwater flow and heat transport are simulated within the blocks.
4) The resulting volumetric temperature of the blocks is evaluated to provide a 3D overview of the thermal state of the subsurface.
5) Using the geological, hydrogeological, and built infrastructure features as inputs and the volumetric temperature of blocks as output, the blocks are statistically clustered into so-called groundwater archetypes with similar features and GWT.
6) Finally, the identified archetypes are classified into geothermal archetypes to showcase a potential application of the approach.

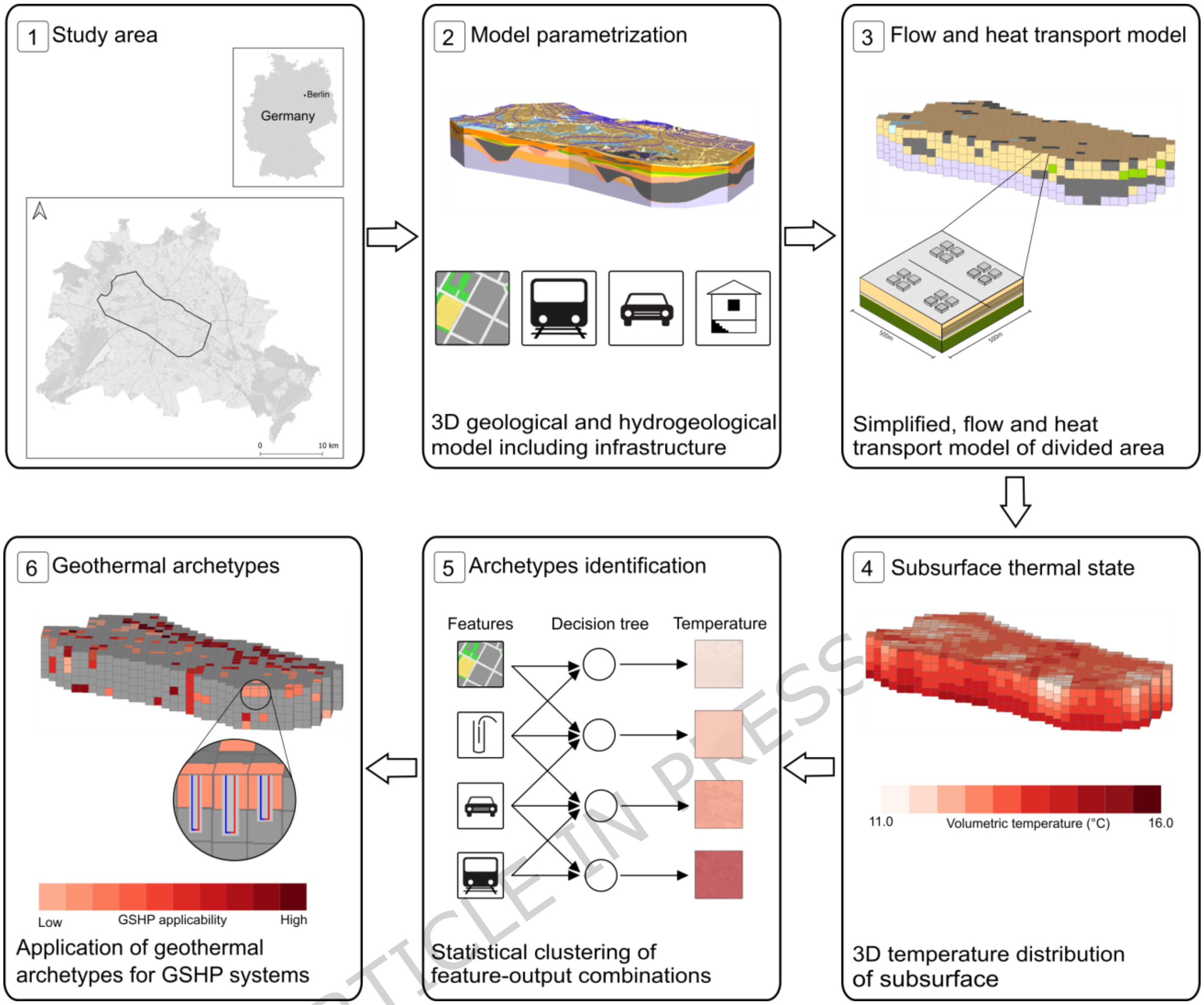

Figure 1: Workflow of geological modelling, groundwater flow and heat transport modelling, groundwater archetype identification and application to geothermal archetypes (i.e., suitability of ground source heat pump).

2.1 Study area and model parametrization

2.1.1 Geological and hydrogeological setting

The study site is located in the urban center of the city of Berlin, Germany, covering an area of around 118 km^2 (Figure 1, step 1). The boundaries of the model are delineated based on groundwater level contour maps as hydraulic boundaries. The eastern and northwestern boundaries of the model are delineated as parallel to the groundwater level contour maps, and the other boundaries are perpendicular to the groundwater level contour maps.

The modeling area lies in the northeastern German basin with a surface geology predominantly characterized by Weichselian glacial sands, deposited in the Warsaw-Barnim glacial valley. The northeastern and southern regions of the model area are formed by glacial tills and marls of the Barnim and Teltow plateaus (Figure 2a). The Rupelian clay forms the lowest layer and functions as the lower aquitard in the model domain, separating the upper freshwater aquifer system and the lower saline water aquifer (Sippel et al., 2013). As a result of North German tectonics, the top of the Rupelian clay varies significantly from -30 m above sea level (asl) in the west to 200 m asl in the southeast of the study area (Göthel and Hermsdorf, 2014).

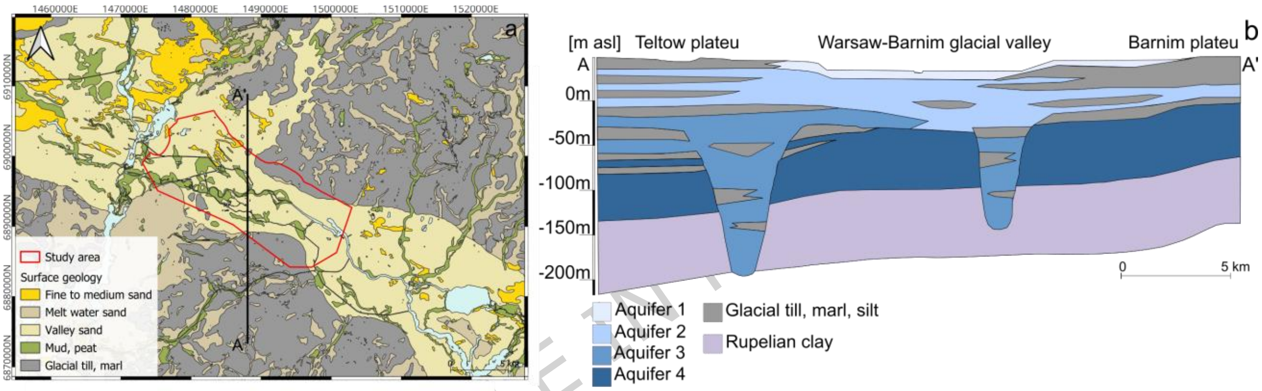

Figure 2: a) Surface geology of the study area, b) Cross section A-A' showing the hydrogeological setting of area and the freshwater Aquifers 1-4 (modified from Limberg & Thierbach, 2002).

The study domain contains four freshwater aquifers (Figure 2b) (Limberg & Thierbach, 1997). The upper aquifer (Aquifer 1) is a large, unconfined aquifer formed by Holocene sands and underlying valley sands of the Weichselian period. The Holocene layer consists of anthropogenic materials as well, resulting in a highly heterogeneous lithology of the uppermost aquifer (Göthel & Hermsdorf, 2014). As a result of several retreats and advances of the continental ice sheets in the Saalian period, alternating layers of glacial till and marl were deposited, interbedded with extensive glaciofluvial meltwater sands which form the Aquifer 2. This second aquifer is, to a large extent, hydraulically connected to Aquifer 1 and is also known as the main aquifer (German:

"Hauptgrundwasserleiter") due to its significance for Berlin's drinking water supply (Limberg & Thierbach, 1997).

Aquifer 3 is hosted in sediments deposited during the Elsterian glaciation and subsequent Holstein interglacial and consists primarily of fluvial to glaciofluvial sands and gravelly sands. These permeable sediments were formed in glacial channels and lake basins but are frequently interrupted by aquitards composed of glacial till, marl, clays, and silts, resulting in a heterogeneous aquifer structure (Göthel & Hermsdorf, 2014). The deepest freshwater aquifer, Aquifer 4, is formed by fine to coarse quartz sands of the Miocene and sands with mica from the upper Oligocene, located above the Rupelian clay, which is the bottom layer of the domain. This Aquifer 4 is in many places hydraulically connected to the upper Aquifers 1-3, where overlaying aquitards are absent and Elsterian channels establish lateral contact (Limberg & Thierbach, 1997).

A detailed 3D geological model is developed in Leapfrog Geo (Seequent, 2024) by importing georeferenced geological cross sections of the study site into the software from the Geoportal Berlin (2024). For the entire area of Berlin, 58 Geological cross sections are available at 1km intervals in north–south and west-east direction each. 22 of those intersect the modeling domain and are used for the geological modeling. These cross sections are available for a maximum depth of 300m bgl. To extrapolate 3D surfaces from the 2D layers obtained from the cross sections, the Leapfrog Geo workflow uses an implicit modelling method. After introducing lithology and their chronology as 3D spatial polyline objects, the cross sections are digitized by hand as accurately as possible. Based on this 2D information, Leapfrog Geo interpolates lithological surfaces and subsequently the volumes that shape the full 3D model. Since there is no independent data, such as additional borehole data, available to assess the accuracy of the model quantitatively, the interpolation algorithm is iteratively modified and compared to the geological cross-sections until a good visual fit is obtained. The surface geology is also incorporated into the model by modifying the initial Leapfrog model using the available surface geological map from Geoportal Berlin (2024). Then, the 3D model domain is split into equally sized blocks (500 m × 500 m × 50 m), resulting in

5 layers of 530 blocks each. Finally, using the Leapfrog Geo's Hydrogeology extension, a 3D finite element template model is constructed. This model is then discretized in Triangular prismatic elements by first creating 2D triangular grids and then extruding it to make a 3D mesh. This mesh was then exported to FEFLOW for automated flow and heat transport modelling.

2.1.2 Built infrastructure within the study area

The study area is located in a densely built-up urban area, both in terms of above and below-surface infrastructures. Thus, incorporating built infrastructure, which affects the thermal and hydraulic state of the subsurface model, is an essential step for obtaining a detailed, large-scale overview of the thermal state of the study area (Figure 1, step 2). Based on data available in the literature (e.g. Epting et al., 2013; Benz et al., 2015; Previati et al., 2022; Noethen et al., 2023), underground car parks (UCP), building basements, underground train tunnels, and the ground surface temperature (GST) are included as anthropogenic features (Figure 3).

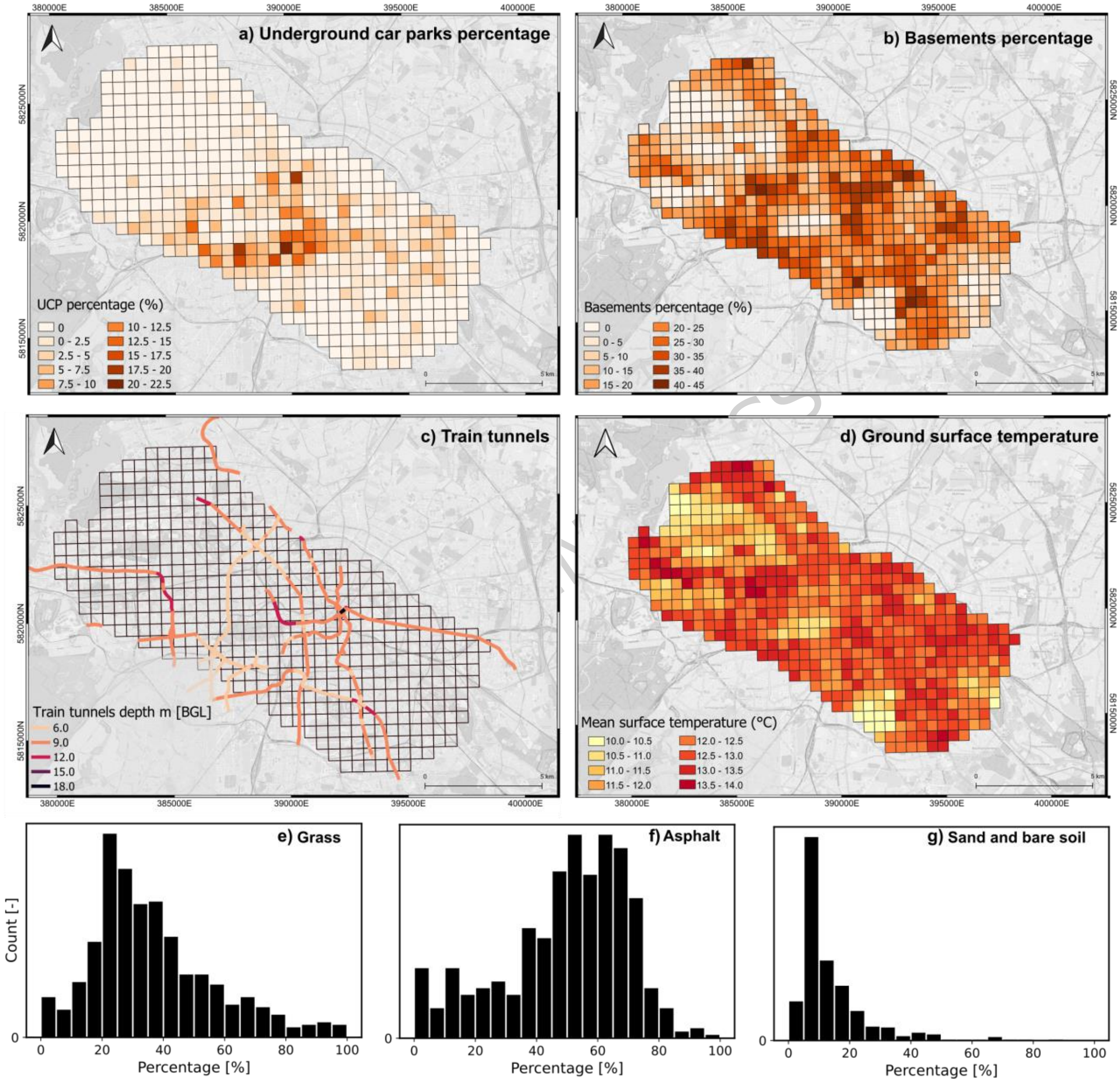

Figure 3: a) Underground car park percentage, b) basement percentage, c) train tunnel presence, d) ground surface temperature, and e-g) histograms of land use classes within each block, used as inputs to flow and heat transport model (Figure 1, step 2)

The distribution of UCP footprints in the modeling domain is shown in Figure 3a as a percentage of area per block based on UCP footprints provided by Noethen et al. (2023). UCPs are unevenly distributed throughout the domain, with a higher concentration being found in the center of the modelled domain, with as much as 23% of the block area being UCP (Figure 3a). However, most of the blocks do not include any UCP. The building density distribution is based on available building footprint data (OpenStreetMap contributors, 2017) (Figure 3b). As there is no complete data on the extent of all basements in the modeling area, all buildings are assumed to have a basement down to 3 m below ground, which reflects the typical value available from the Geoportal Berlin (2024). Figure 3b highlights some highly urbanized locations with up to 45% of basements in the center of the modelled domain. Nonetheless, a notable portion of the study area comprises green spaces or underutilized land, where building and basement coverage is comparatively low. Train tunnel density, including subway (Berliner U-Bahn) and regional train (S-Bahn) tunnels within the domain, is depicted in Figure 3c, showing horizontal layout of the train tunnels and the corresponding depths below ground. The tunnels are represented in five specific depth intervals: 6, 9, 12, 15, 18 m below ground level (bgl) (OpenStreetMap contributors, 2017). Most of the blocks do not contain any train tunnels, while a few blocks contain multiple train lines at different depths, especially around the center of the domain near the dense area of Alexanderplatz, where multiple transport lines connect.

The spatial distribution of GST is shown in Figure 3d, calculated according to a method from Benz et al. (2015), where land use data (Geoportal Berlin, 2024) is translated to GST according to different surface materials: grass, asphalt, and sand and bare soil. For each block, the percentage of these surface materials was calculated based on the land use type. The minimum temperature difference between air and soil for each material type (0.2, 1.5, and 4.0 °C for grass, sand and bare soil, and asphalt, respectively) is then added to the annual mean air temperature of 9.9 °C (Deutscher Wetterdienst, DWD) to compute surface type-specific GST values. Subsequently, a weighted average, annual mean GST is calculated based on the share of each land use type within individual blocks. Accordingly, higher GST values are assigned to densely built-up areas, which cover the majority of blocks, and lower GST for green and open areas with larger grass and sand (e.g., Tiergarten and former Tegel airport), and bare soil portions (Figure 3d). The obtained spatial distribution of GST values using the minimum difference from Benz et al. (2015), with an average temperature of 12.3°C, is reasonably close to surface temperature data from the MODIS satellites, with an average temperature of 12.2°C. The MODIS data itself, however, has a resolution lower than the block models (1 km × 1 km) and is therefore not directly used. Histograms showing the share of land surface materials provide further insight into surface material coverage within the blocks. The distribution of grass percentage within blocks exhibits a mild left skew, indicating that, while a few blocks have a high percentage of grass, most of them contain few to moderate green areas (Figure 3e). The asphalt distribution, in contrast, is right-skewed, reflecting the predominance of impervious human-made surfaces in the modeling area (Figure 3f). A very low coverage of sand and bare soil in the model domain is observed with a sharply left-skewed histogram, revealing that this surface type is rare and limited to a few blocks (Figure 3g).

2.2 Flow and heat transport modeling

In the third step, 3D steady-state numerical models are built for each block in FEFLOW (Diersch, 2014) to calculate block volumetric GWT for further analysis and archetype identification. Within each block model, hydraulic and thermal properties are assigned based on lithologies derived from the 3D geological model (Table 1). Since it is not possible to directly export the block-level lithology from Leapfrog Geo to FEFLOW, blocks are instead parametrized according to their geological composition. To this end, lithologies within each block are assigned in a layered sequence, ordered from oldest to youngest formation.

Table 1: Hydrogeological input parameters and values used for flow and heat transport models.

Geological unit	**Predominant lithology**	**k_f (m/s) [a]**	**n_e (-) [b]**	**c_h (MJ/m^{3}K) [c]**	**$c_{h,\ unsat}$ (MJ/m^3 K) [c]**	**λ (W/m K) [c, d]**	**λ_{unsat} (W/m K) [c, d]**
Holocene	Peat, mud, silt	1.0×10^{-7}	0.07	2.0	0.8	0.4	0.4
Weichsel	Valley sand, meltwater sand, gravel	1.4×10^{-5}	0.2	1.6	1.6	1.8	0.4
H2 (Weichsel)	Glacial till	1.0×10^{-6}	0.05	1.5	2.0	2.9	2.9
Saale	Meltwater sand, gravel	4.0×10^{-6}	0.2	1.6	1.6	1.8	0.4
H3.1-H3.2 (Saale)	Glacial till, silt, clay	1.0×10^{-6}	0.04	1.5	2.0	2.9	2.9
Holstein	Gravelly sand	4.0×10^{-6}	0.2	1.7	0.8	0.4	0.4
H3 (Holstein)	Silt, mud, clay	1.0×10^{-8}	0.04	2.2	0.8	0.4	0.4
Elster	Meltwater sand	8.9×10^{-7}	0.2	1.6	1.6	1.8	0.4
H4 (Elster)	Glacial till, silt, clay	1.0×10^{-6}	0.04	1.5	2.0	2.9	2.9
Miocene	Quarzsand	1.0×10^{-6}	0.12	1.6	1.6	2.7	0.4
H5 (Miocene)	Silt, clay	6.8×10^{-7}	0.04	1.5	1.5	2.5	0.4
Oligocene	Fine sand with mica	1.1×10^{-6}	0.12	1.7	1.6	2.6	0.4
Rupelian Clay	Clay	1.0×10^{-9}	0.003	2.2	1.6	1.5	0.5

Values derived from [a] Limberg and Thierbach (2002), [b] Hölting and Coldway (2013), [c] Frick et al. (2019), [d] VDI 4640 (2010).

k_f: hydraulic conductivity; n_e: effective porosity; c_h: heat capacity; $c_{h,\ unsat}$: unsaturated heat capacity; λ: solid thermal conductivity of solid; λ_{unsat}: unsaturated thermal conductivity of solid.

The official hydraulic head contour map of Berlin (Geoportal Berlin, 2024) is used to define the hydraulic boundary conditions (BCs) along the modeling domain, and accordingly to the outer blocks (Figure 4a). The hydraulic BCs of the model are implemented using the groundwater contour maps of the main aquifer (Aquifer 2). The close-standing hydraulic head contours in the northern and northeastern regions of the model domain indicate steep hydraulic gradients, suggesting potentially high groundwater flow velocities in this area. Here, groundwater predominantly flows from the northern and northeastern areas of the model domain towards the central and southeastern areas. Hence, the northern and northeastern boundaries (and the corresponding blocks) are considered hydraulically as inflow, and the northwestern boundary as an outflow boundary. In accordance with the groundwater contours, the southern, southeastern, and parts of the northern boundary are assumed to be no-flow boundaries (Figure 4a).

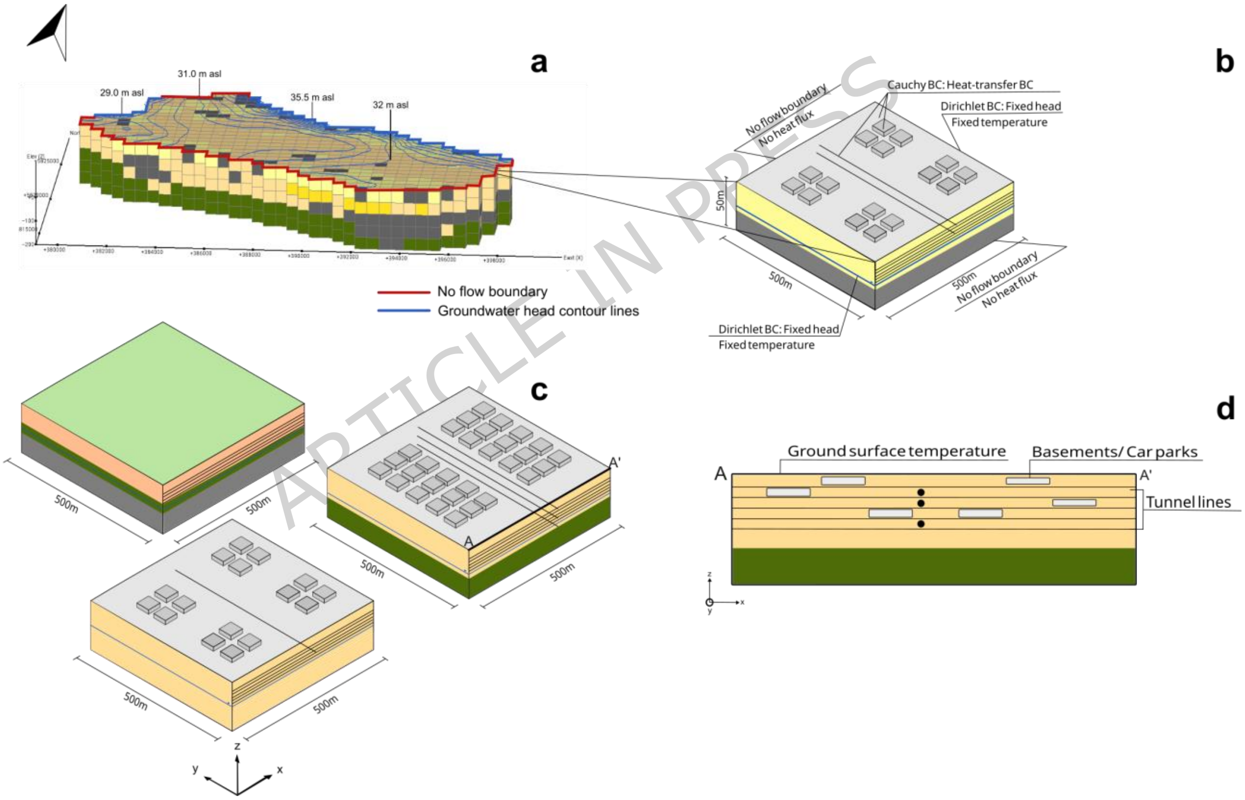

Figure 4: a) Block-divided modeling area with hydraulic and thermal boundary conditions, b) conceptual model of blocks, c) conceptual model of boundary condition (BC) variations within study area, d) cross-section A-A'. The conceptual model is the basis for the flow and heat transport model (Figure 1, step 3).

A Dirichlet head BC is applied to two opposite boundaries of each block using the head difference derived from the hydraulic head contour map. The two remaining sides of the blocks are assumed as no-flow boundaries (Figure 4b). This boundary configuration allows for a simplified representation, while regional groundwater flow patterns guide the order of simulations and the upstream temperature BC assignment. To calculate the magnitude of inflow from upstream blocks, the average head level for Aquifer 2 in each block is calculated. For the sake of simplicity, a head difference of > 0.5 m is used to distinguish between adjacent blocks that are hydraulically connected from those that are simulated without upstream (or downstream) connectivity.

Initially, the blocks on the border of the model area are assigned a fixed temperature as the thermal BC using GWT measurement data (Geoportal Berlin, 2024). The next group of blocks simulated are the blocks without a flow into them. The no-flow blocks are also assigned a constant initial temperature using the measurement results at all boundaries to account for the thermal effect of surrounding blocks. Having run the boundary blocks and the no-flow blocks thus determined the outflow (or downstream) temperature; this temperature is set as the inflow (or upstream) temperature for the hydraulically connected blocks downstream. The upstream temperature of blocks with more than one connected upstream block is calculated as the weighted average of the downstream temperature of the upstream blocks based on the hydraulic head difference between the adjacent blocks in each direction.

To account for thermal input from basements and UCPs (Figure 3a, b), these are implemented as Cauchy BC. Each UCP is assumed to have a 3 m depth and a constant temperature of 18°C (Noethen et al., 2023). Based on the percentage coverage of UCP within each block, the effective area is calculated, and the temperature BC is assigned accordingly to the model mesh. The same applies to basements, which are also assumed to have a depth of 3 m. Since there is no information on whether basements are heated or not, a typical average temperature of 15°C was assumed for all basements to represent both heated and unheated basements (Hoffmann & Geissler, 2017).

For each block intersected by train lines (Figure 3c), a train tunnel is incorporated with a width of 8 m and height 4 m and a length of 400 m, implemented centrally parallel to the y-axis (Figure 4b). A constant temperature of 18°C is assigned to the train tunnels (Sun et al., 2021). All anthropogenic infrastructures are assumed to be impervious with a very low hydraulic conductivity of 1.0×10^{-16} m/s (Epting et al., 2013).

The amount of heat flow from infrastructure (i.e., basements, UCPs, and tunnels) to the subsurface depends on the thermal conductivity of the material (e.g., concrete) divided by the wall or slab thickness of the structure, referred to as the heat transfer coefficient in FEFLOW. The thermal conductivity and heat capacity of concrete are assumed to be 1.8 W/(mK) and 1.6 MJ/m^{3}K, respectively (Makasis et al., 2021). The heat transfer coefficient was calculated following the approach introduced by Noethen et al. (2023) and is 0.02 W/(m^{2}K). In this calculation, the thicknesses of structure walls and slabs for basements and UCPs are assumed to be 0.3 m and 0.5 m, respectively, and those for train tunnels are assumed to be 0.5 m.

The calculated GST value for each block is also considered as a Cauchy BC on top of the block models. The vertical heat flux from the ground surface into the subsurface is again implemented by a heat transfer coefficient. This coefficient for the upper BC is calculated utilizing unsaturated zone thickness obtained from hydraulic head and topography data, as well as thermal conductivity. Fixed temperature values (15.1°C to 16.4°C) are applied at the bottom of the deepest layer of block models based on available measurements (Geoportal Berlin, 2024) and using temperature gradient values from deep temperature profiles (Blum et al., 2021).

To perform the block simulations, model input files for FEFLOW with the assigned boundary conditions are iteratively generated in Python based on a template model and then simulated in FEFLOW. A central and symmetric configuration of basements and UCPs is adopted to speed up the iterative process and ensure simplicity of the model generation, while preserving the essential thermal influence of anthropogenic structures. Overall, each block model consists of 249,800 elements for the uppermost layer of blocks with dense built infrastructure (i.e., 0-50 m bgl). A finer discretization was applied around each UCP, basement, and train tunnel. In contrast, for the four deeper layers of blocks, coarser discretization was used, resulting in 58,960 elements across these blocks.

2.3 Archetypes identification

Based on the results from the block modelling, the groundwater archetypes are identified (Figure 1, step 4). To this end, an input-output dataset is prepared that contains all input features, i.e., hydrogeological parameters and built infrastructure properties of each block. The specific feature combinations of all blocks serve as input, and their simulated volumetric temperatures as the corresponding output. Subsequently, a regression-based decision tree algorithm is employed on the input-output dataset to cluster the blocks into so-called archetypes. The decision tree algorithm is discussed in detail in Hastie et al. (2009).

Decision tree construction starts with splitting the input-output dataset at the first node based on the feature that reduces the mean squared error (MSE) of the volumetric temperature values the most. The splitting process continues, guided by the tolerance value, which represents a threshold value for the minimum acceptable MSE or impurity reduction, until a low global impurity (i.e., low overall MSE across all leaf nodes) is achieved. The tolerance value is therefore a critical parameter in selecting the number of leaf nodes of the decision tree, which represent the archetypes in our approach. These are characterized by a distinct combination of input features and thermal state (i.e., simulated GWT). For the uppermost layer of blocks, the input features include hydrogeological and anthropogenic infrastructures. However, the deeper layers without any infrastructure only include (hydro)geological features as input for the decision tree analysis. Thus, the decision tree analysis is performed separately for the uppermost layer of blocks (0-50 m bgl) and the four deeper rows of the blocks (50-250 m bgl).

3 Results and discussions

3.1 3D geological and hydrogeological model

The 3D geological model built using Leapfrog Geo consists of 14 lithologies (Figure 5a). To assess geological model accuracy, the available input cross sections were tested against cross sections extracted from the simulated geological model (Figure 5b) at similar coordinates. As the Leapfrog algorithm does not exactly interpolate the lithologies based on the input cross-section, the cross-sections were verified against the same input cross-sections. Furthermore, the surface geology map (Geoportal Berlin, 2024) was used to verify the initial geological model. The visual comparison indicated a good agreement between the cross sections based on borehole data and the modelled ones, as well as the surface geology map, confirming the reliability of the 3D geological model. It should be noted that rigorous validation of the geological model based on independent data would improve the robustness of the model and increase confidence in the approach. This could, for example, be achieved by using the original borehole data (instead of pre-processed 2D cross-sections) and a test-training split in areas where such data is readily available. Also, as commonly done for deep, basin-scale geological models, additional geophysical data, e.g. from shallow electrical resistivity tomography (Alao et al., 2024) could be used for validation purposes in the future.

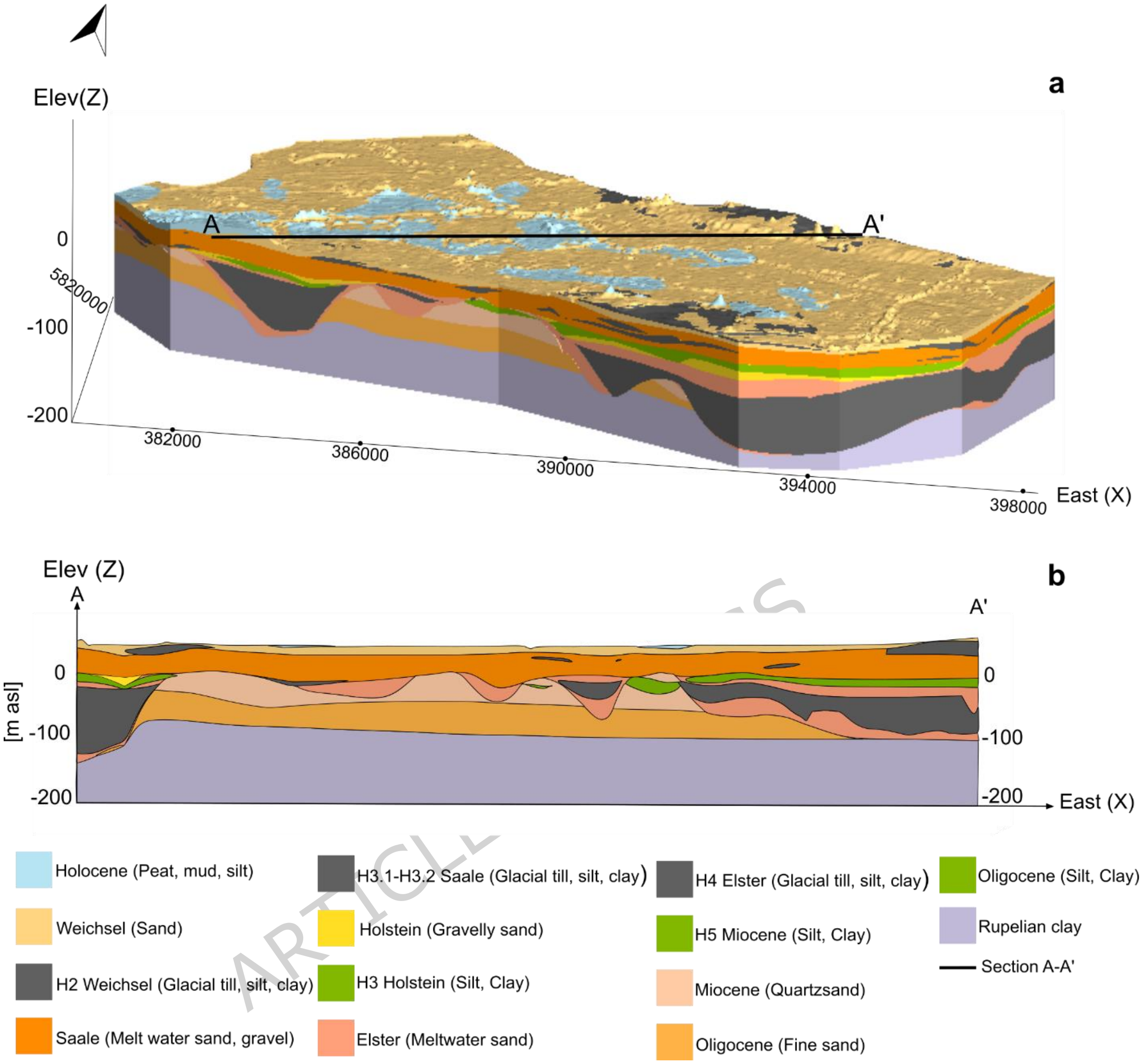

Figure 5: a) 3D geological model and the study area as the basis for groundwater flow and heat transport models, b) cross-section view A-A'

Analysis of regional groundwater flow patterns based on the average head level for Aquifer 2 in each block reveals a significant spatial variability of groundwater flow direction across the modelling domain, leading to complex hydraulic interactions between neighboring blocks in some areas (Figure 6). Some blocks are located in areas with significant inflow (and outflow) of groundwater, while others exhibit no groundwater flow. Blocks along the northern and northeastern edge (mostly around the Barnim Plateau), as well as a few blocks in the center of the area, exhibit significant flow conditions, are hydraulically and also thermally connected. In contrast, many of the central blocks, as well as blocks on the south and southeast, do not show significant flow conditions and are therefore not hydraulically connected.

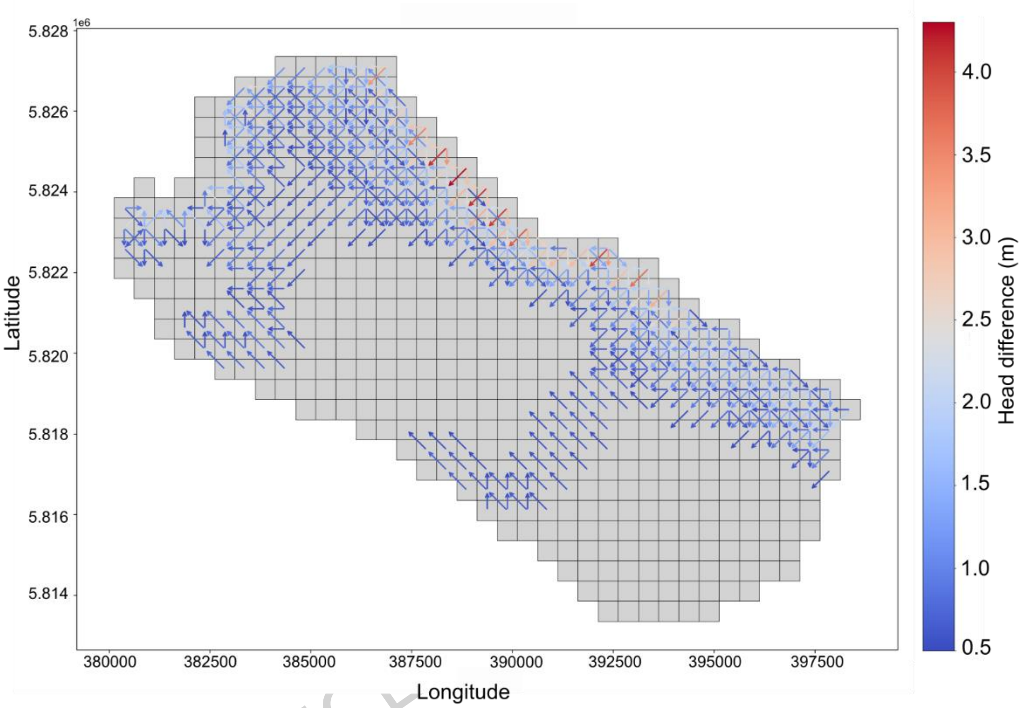

Figure 6: Connectivity graph showing direction of groundwater flow and hydraulic connections between the blocks. The color indicates the magnitude of groundwater flow by showing the hydraulic head difference in Aquifer 2 (main aquifer) across the blocks. The graph guides the simulation order of blocks for subsequent flow and heat transport modeling.

3.2 Flow and heat transport model

Following the simulation of groundwater flow and heat transport in all blocks guided by the connectivity graph (Figure 6), the volumetric temperature of each block is determined by averaging the modelled GWT across the entire block. Assembling these temperatures across the domain yields a 3D visualization of the thermal state of the subsurface (Figure 7a). Given that the features impacting the subsurface thermal state are different in the uppermost layer and the deeper layers, the two sets of blocks will be further assessed and discussed separately.

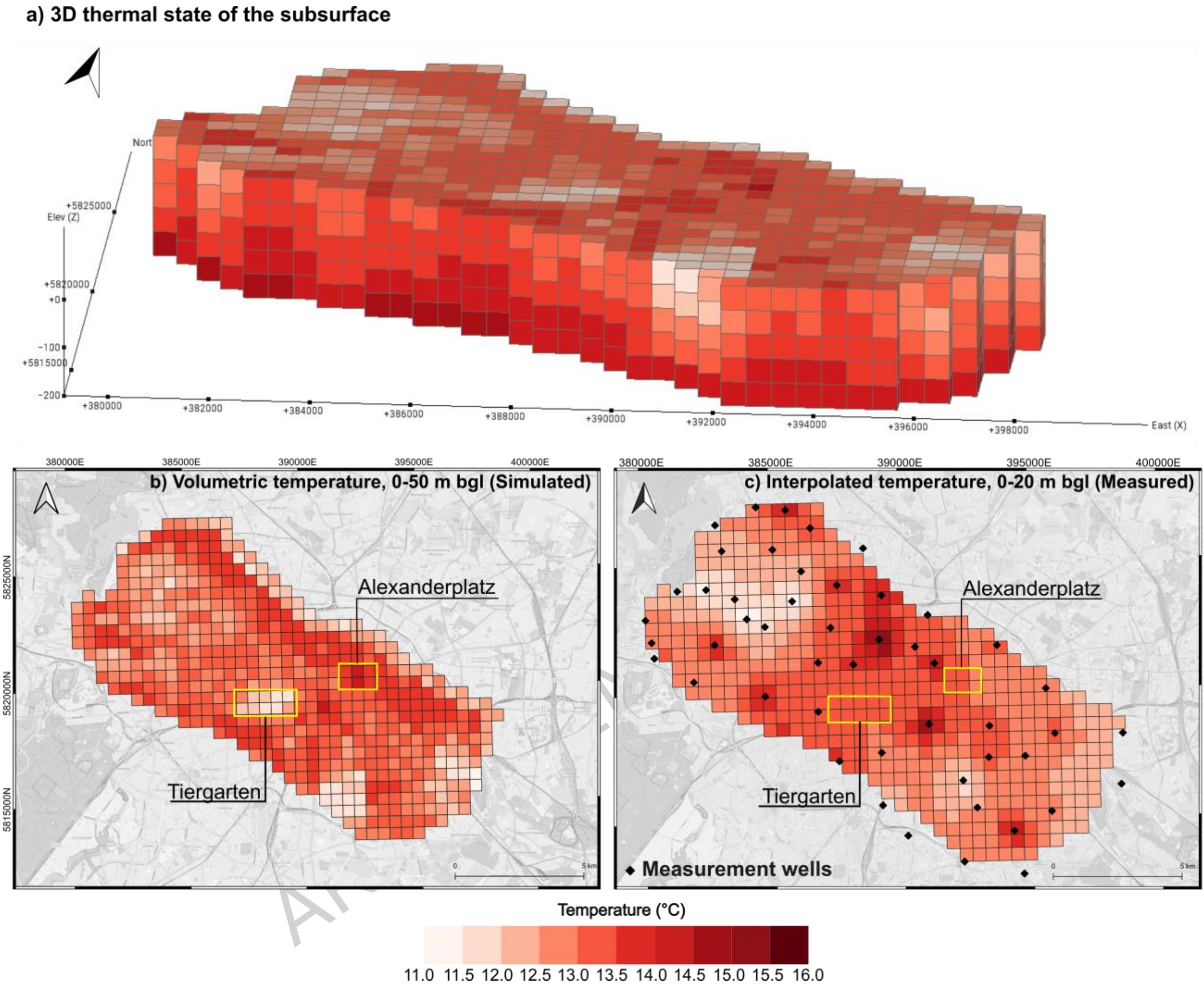

Figure 7: a) 3D groundwater temperature distribution using volumetric temperature of simulated blocks, b) simulated volumetric temperature of the uppermost layer of blocks (0-50 m bgl), and c) groundwater temperature within each block from interpolated maps with the location of measurement wells included at a depth of 20 m bgl.

3.2.1 Near-surface layer of blocks

The near-surface layer of blocks (0-50 m bgl) includes all subsurface anthropogenic infrastructure within the modelling area. The highest temperature values, as expected, are simulated in areas with dense infrastructure and highly used urban areas, mostly around the Berlin Mitte district, Berlin main station, and Alexanderplatz (Figure 7b, cf. Figure 3). Low volumetric temperature values, on the other hand, are obtained for blocks that are less anthropogenically impacted and that are dominated by the green areas, for example, in the Northwest (former airport Tegel), Southeast (Treptower park), Southwest (Tempelhofer Feld), as well as in the center (Tiergarten park).

The effect of anthropogenic heat sources on GWT is in good agreement with findings from previous studies. The number of heated basements that reach into the aquifer is a main factor for higher groundwater temperatures in urban areas compared to rural areas (Menberg et al., 2013; Epting et al., 2013). The heat input from buildings, surface sealing, and tunnels were also found to be the dominant contributors to heat accumulation in the subsurface of the city of Milan (Previati et al., 2022). Other anthropogenic heat sources like UCPs also cause significant GWT anomalies with greater heat fluxes observed in areas where UCPs are denser and deeper (Noethen et al., 2023).

Furthermore, the effect of the upstream temperature is visible in the boundary blocks of the model, in particular along the eastern border of the model domain, where significant hydraulic gradients occur (Figure 7b). High groundwater flow velocities in these regions cause transport of groundwater with higher temperatures along the hydraulic head gradient through the connectivity of the blocks (Figure 6). Accordingly, heat is transported towards the middle of the domain, where it accumulates in blocks with little to no groundwater flow. The effect of groundwater flow on temperature distribution was also observed in previous studies. For example, horizontal advection was shown to be the dominant heat transport process in the urban area of Cologne (Zhu et al., 2015), and GWT in highly dense urban areas is strongly influenced by relative position (downstream or upstream) and distance to anthropogenic heat sources (Ferguson & Woodbury, 2007; Zhu et al., 2015).

Interpolated GWT maps derived from the in-situ measurements in 2024 at 20 m bgl are presented in Figure 7c, together with the well locations of the GWT measurements (Geoportal Berlin, 2024).

The measured temperatures were spatially interpolated and averaged within each block to generate a map to act as a reference for model assessment. The overall large-scale pattern of modelled GWT in the shallowest layer of blocks (Figure 7b) agrees well with interpolated maps from measurements (Figure 7c). However, the GWT values obtained from the block models tend to be slightly higher than the interpolated GWT. The average modelled temperature for all shallow blocks is 13.4°C, while the average interpolated temperature for all blocks from measured data is 12.8°C. Since very few GWT measurements were performed below 50 m, this comparison is only performed for the shallowest layer of blocks.

The observed discrepancy in GWT may stem from several uncertainties in the model. These could be either due to the assumptions made, such as for the heated basement temperature or the hydrogeological properties of the subsurface, which were adopted from literature. It could also be caused by a bias in the location of measurement wells used for interpolation. These wells are often located in small, open green spaces next to streets, and rarely placed directly next to a building or UCPs, nor in the close vicinity of tunnels. As a result, the measured GWT likely does not correctly reflect locally elevated temperatures around or below anthropogenic infrastructure. Furthermore, uncertainties could arise from the interpolation method itself, which can smooth out localized anomalies and inaccurately reflect areas with insufficient data coverage (Menberg et al., 2013).

Despite the general discrepancies, the simulation results indicate local hot spots and low spots. Notably, elevated temperatures are observed around Alexanderplatz (with an average GWT of 14.3°C for blocks involved), an area characterized by the presence of multiple basements and UCPs and five layers of train tunnels. Conversely, lower temperature blocks were simulated for the Tiergarten location (with the average GWT of 12.1°C), where few subsurface structures are present, and the majority of the surface is covered by green spaces. These local low and hot spots could not be detected in the interpolated maps due to the absence of measurement wells in those areas. Yet, those local thermal anomalies are expected based on the surface and subsurface use and measurements at a well in similar areas, as reported in previous studies. For example, in Munich, the recorded GWT around locations of Englischer Garten Park and Nymphenburger Schlosspark were relatively lower than in dense urbanized areas (Böttcher & Zosseder, 2022). Also, GWT measurements in other cities like Karlsruhe (Menberg et al., 2013) and Cologne (Menberg et al., 2013; Zhu et al., 2015) found higher GWT in wells close to dense infrastructure.

3.2.2 Deeper layers of blocks

Deeper blocks, i.e., at depths greater than 50 m, in the model do not contain built infrastructure (yet), and their modelled thermal state (i.e., volumetric temperature) is primarily influenced by adjacent blocks through upstream GWT conditions (Figure 8). The temperature range for depths of 50-100 m bgl varies between 12.0°C and 14.6°C. The temperature distribution at this depth range still indicates a notable spatial heterogeneity, reflecting the trend of near-surface blocks and heat input from the block layer above. Accordingly, the thermal impact of densely built-up (e.g., main train station) or large green areas (e.g., Tiergarten, Tempelhofer Feld) from the uppermost block is still visible at this depth. Such subsurface thermal impact was also observed in previous studies, notably by Bidarmaghz et al. (2020), who simulated anthropogenic heat impacts extending to a depth of up to 70 meters. Previous studies in Berlin also showed that the influence of anthropogenic heat sources on measured GWT extends down to depth of 50-100 m bgl (Bayer et al., 2019; Blum et al., 2021).

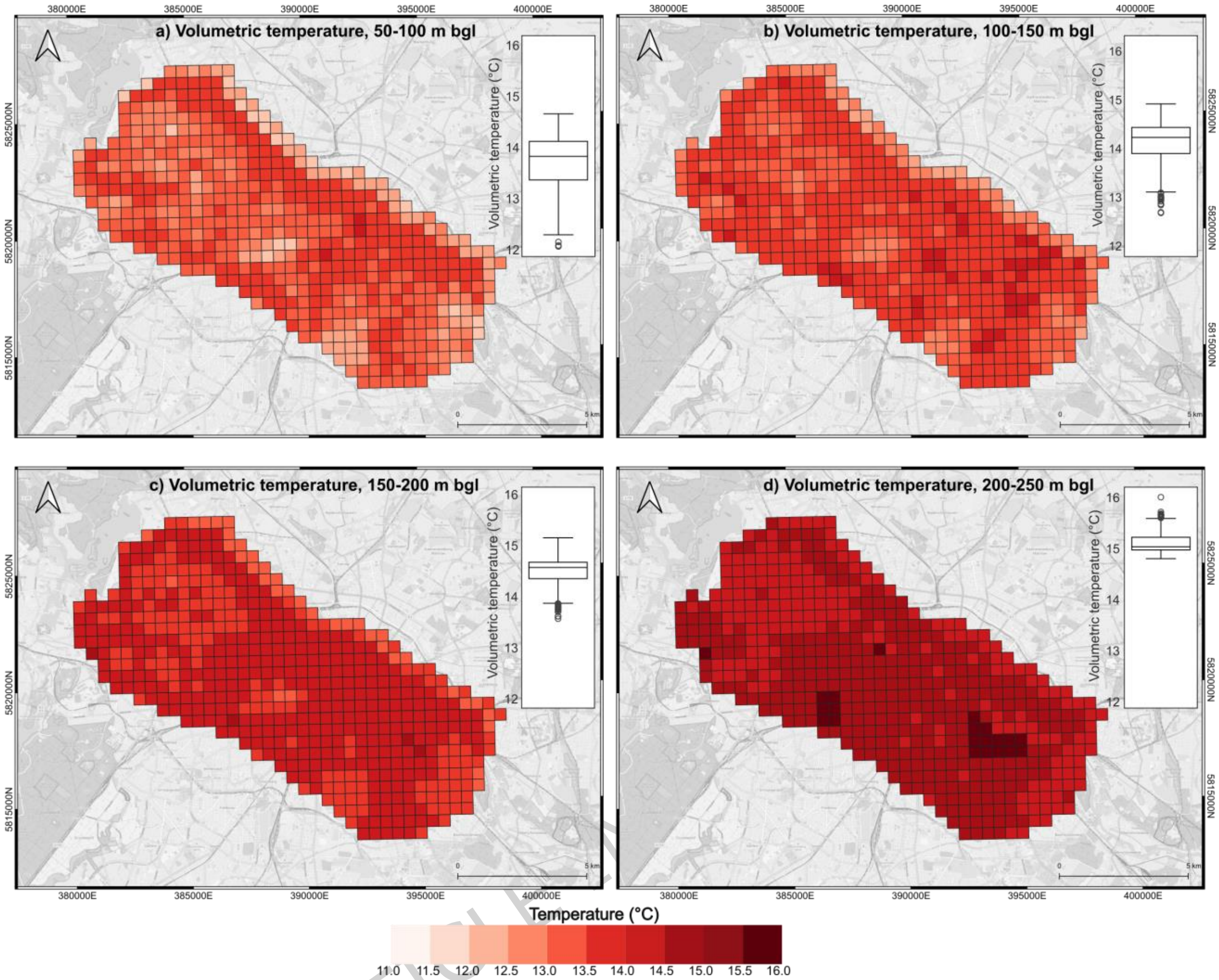

Figure 8: Volumetric temperature of the deeper layers of blocks at a) 50-100 m, b)100-150 m, c) 150-200 m, and d) 200-250 m bgl. Box plots indicate distributions of volumetric temperature for each depth interval.

At a depth of 100-150m bgl, the simulated volumetric temperatures range from 12.7°C to 14.8°C. The spatial distribution shows a pattern similar to the upper layers of blocks, but with a narrower range, indicating a decrease in thermal heterogeneity. Between 150-200 m bgl, the temperature range increases slightly, ranging from 13.6°C to 15.2°C. However, temperature changes within this range remain limited, suggesting diminishing influence from shallower anthropogenic drivers and a thermally buffered environment. At the deepest layer of blocks, i.e., 200-250 m bgl, temperature ranges from 14.8°C to 16.0°C, with a highly uniform spatial distribution. The homogeneity of temperature distributions at this depth suggests that the modelled subsurface thermal regime is mainly governed by regional geothermal gradients rather than near-surface anthropogenic influences.

Overall, the modelled temperature distribution suggests a progressive geothermal effect with increasing depth. The increasing homogeneity of the temperature variation at greater depths can be attributed to the subsurface hydrogeological conditions, in addition to the diminishing influence of near-surface structures. In particular, the deeper blocks are predominantly composed of Rupelian clay, a formation with a lower hydraulic conductivity (1.0×10^{-9} m/s), limiting the lateral spread of temperature plumes and causing a more stable thermal regime. These findings align well with deep measured temperature profiles reported in earlier studies (Blum et al., 2021; Frick et al., 2019; Bayer et al., 2019; Ferguson & Woodbury, 2007).

3.3 Archetypes identification

3.3.1 Near-surface layer of block models

After simulation of all blocks, the calculated volumetric temperatures are used to prepare the input-output dataset for archetype identification via decision tree analysis. With increasing tolerance values (i.e., the threshold value for the minimum acceptable impurity reduction), the number of obtained archetypes decreases (Figure 9, left axis). Changing the algorithm tolerance also affects the average node impurity over all leaf nodes (Figure 9, right axis). To investigate the influence of algorithm tolerance on the number of archetypes, as well as their spatial distribution, four different values of algorithm tolerance, as well as the corresponding number of archetypes and values of node impurity, are investigated in detail below. Nevertheless, regardless of the slight fluctuations in the tolerance value, overall node impurity remains low (0.05-0.13°C), indicating robustness of the decision tree analysis. The low MSE is comparable to the node impurity in a previous archetypes study, where it was in the range of 0-0.06 °C (Kreitmair et al., 2023).

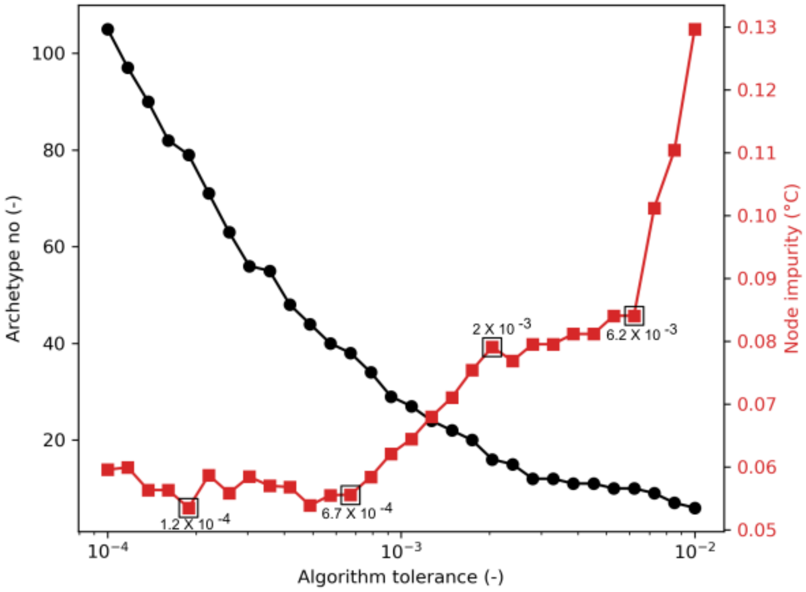

Figure 9: Number of archetypes identified (left axis) and node impurity value calculated as MSE (right) for a given algorithm tolerance for the shallow blocks (0-50 m bgl).

The results of the decision tree are evaluated accordingly at the four selected tolerance values (highlighted in Figure 9), and the spatial distribution of the groundwater archetypes results are visualized with respect to the archetype temperature in Figure 10a-d. Therefore, instead of showing the temperature calculated for each block model, Figure 10 shows the aggregate temperature of each archetype representing multiple blocks. In accordance with Figure 9, the number of identified groundwater archetypes reduces with increasing tolerance. The average predicted volumetric temperature for all number of archetypes (i.e., 10, 17, 38, and 82) is 14.4°C, which is equal to the simulated volumetric temperature (Figure 7b). Yet, even with a small number of archetypes, such as 10 (Figure 10d), the overall spatial pattern of GWT distribution is similar compared to the results with 82 archetypes (Figure 10a), and also similar to the initial GWT modeling results (Figure 7a), which again demonstrates the robustness of the decision tree analysis.

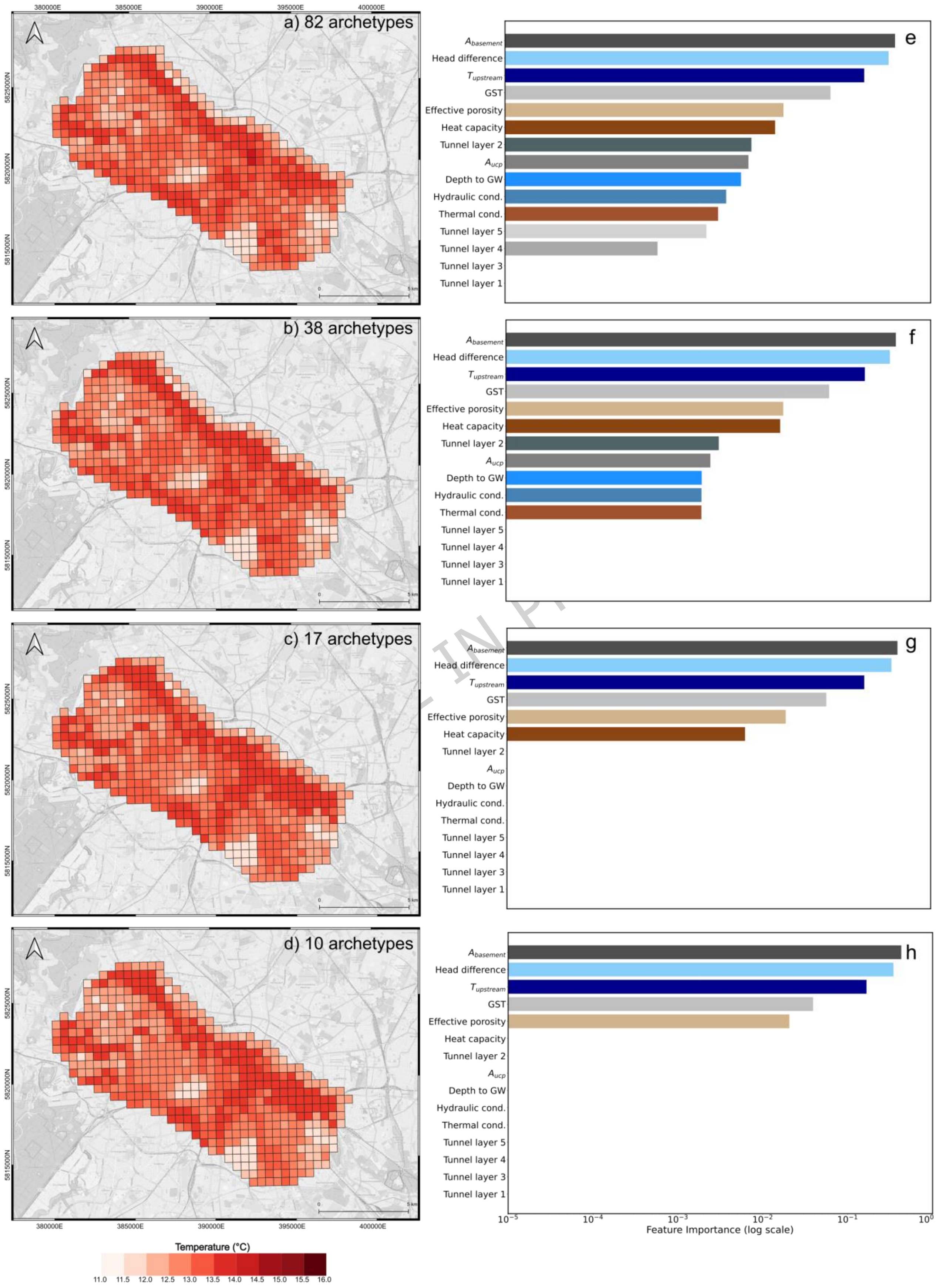
a) 82 archetypes
b) 38 archetypes
c) 17 archetypes
d) 10 archetypes
380000E
385000E
390000E
395000E
400000E
5825000N
5820000N
5815000N
0
5 km
Temperature (°C)
11.0
11.5
12.0
12.5
13.0
13.5
14.0
14.5
15.0
15.5
16.0
e
f
g
h
$A_{basement}$
Head difference
$T_{upstream}$
GST
Effective porosity
Heat capacity
Tunnel layer 2
A_{ucp}
Depth to GW
Hydraulic cond.
Thermal cond.
Tunnel layer 5
Tunnel layer 4
Tunnel layer 3
Tunnel layer 1
10^{-5}
10^{-4}
10^{-3}
10^{-2}
10^{-1}
10^{0}
Feature Importance (log scale)

Figure 10: (a)-(d) Temperature of shallow (0-50 m bgl) subsurface for different numbers of archetypes, based on different tolerance values highlighted in Figure 9, and (e)-(f) corresponding feature importance.

The influence of the number of archetypes selected on the features contributing to the formation of archetypes is shown in detail in the feature importance plots (Figure 10e-h). Heated basements consistently emerge as the most significant feature in creating the archetypes. This is not surprising based on the high density of basements in the model domain (Figure 3b). Several studies have previously demonstrated the influence of heated basements on groundwater temperature in urban environments (Attard et al., 2016; Epting et al., 2013; Ferguson & Woodbury, 2007; Kreitmair et al., 2023; Rock & Kupfersberger, 2018).

Groundwater head difference and upstream temperature also play a significant role in splitting decision tree nodes, specifically for the blocks that have significant groundwater flow. Groundwater head difference mainly influences the heat transport by advection, which is particularly important for regions with high groundwater flow velocity. This is consistent with previous findings showing that, when advection is the dominant process, heat transport is primarily downstream (Zhu et al., 2015). Another critical feature contributing to archetype identification is ground surface temperature, which affects vertical heat flux into the subsurface and accordingly influences shallow subsurface thermal distributions. The effect of surface temperatures on the GWT distribution was quantitatively assessed in previous studies (e.g., Menberg et al., 2013, and Benz et al., 2015), who demonstrated that urban surface heating can be a significant source of anthropogenic heat flux into the shallow subsurface.

Among the geological and hydrogeological properties, heat capacity and effective porosity play a substantial role in identifying the archetypes. These parameters are among the most important features contributing to temperature distribution, as also found by Kreitmair et al. (2023). UCPs and train tunnels also influence the groundwater archetypes identification. The impact of UCPs and train tunnels on GWT anomalies in densely built areas has been widely reported previously (Noethen et al., 2023; Previati et al., 2022).

In contrast, several features appear to play no part in the decision tree divisions. One explanation for such zero importance values can be correlation between features. For instance, thermal conductivity and heat capacity are physically closely related, and the decision tree algorithm may select only one of them to split the nodes (e.g., heat capacity), while assigning zero importance to the other (e.g., thermal conductivity) (Figure 10 g-h). Another reason could be a high number of zero values for a specific feature across the modeling domain (and, accordingly, the input-output dataset). For example, a feature such as tunnel layer 4, which is present in only one block (out of 530 in the shallowest layer), provides limited information for the decision tree and thus is not selected during decision tree building process, or only for very low tolerance values.

Overall, the number of archetypes used for further analyses should be chosen carefully, in order to balance computational efficiency and accurate representation. Too many archetypes would impact the computational time of further analyses (i.e., through a larger number of detailed numerical simulations), and too few archetypes would lead to a merging of distinct thermal and hydrogeological behavior of different blocks. Accordingly, extreme cases such as 10 and 82 archetypes are excluded from the final selection, while an intermediate number of archetypes between 17 and 38 is deemed more suitable.

Moreover, the number of archetypes for management purposes should be selected strategically, based on management objectives. For instance, comparing the temperature distribution between the threshold options with 38 archetypes (Figure 10b) and 17 archetypes (Figure 10c) reveals that tunnel layer 2 emerges as a distinguishing feature in clustering the blocks (Figure 3c, especially blocks intersected by tunnel layer 2). This suggests that selecting 38 archetypes enhances the ability to identify the effect of such infrastructures, thereby enabling more targeted analysis.

3.3.2 Deeper layers of block models

The four deeper layers of block models (50-250 m bgl) include no anthropogenic infrastructure. Thus, the regression-based decision tree to identify archetypes was run using the temperature BC (lateral, upper, and lower boundaries) and hydrogeological parameters (thermal conductivity, hydraulic conductivity, etc.) as inputs and the volumetric temperature as output. In order to balance the number of archetypes generated and the overall model error, a tolerance value of 2×10^{-4} was selected. This resulted in 21 distinct archetypes and a low value of MSE of 0.01°C (Figure 11a).

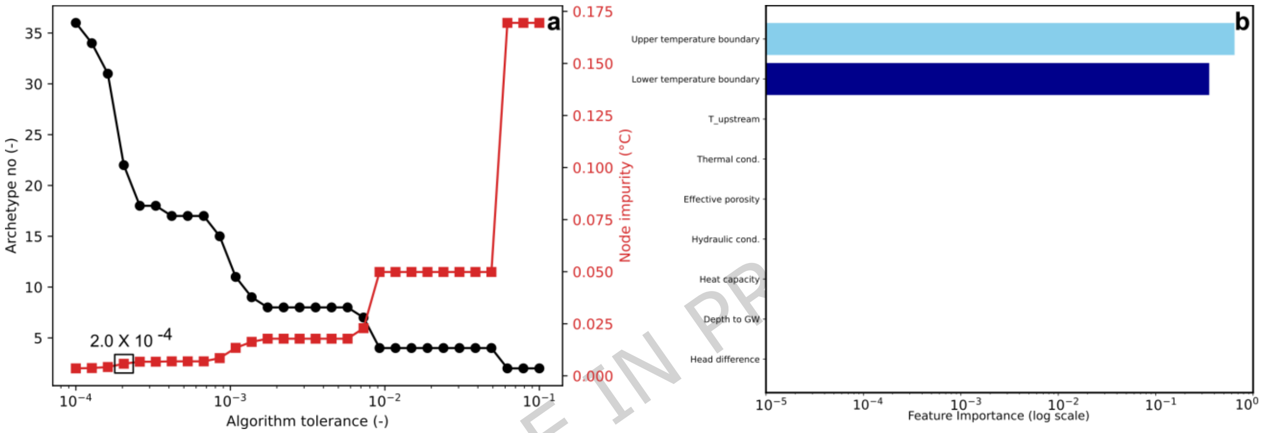

Figure 11: a) Algorithm tolerance to find the optimum number of archetypes vs the node impurity calculated as MSE, and b) the feature importance plot for the deeper blocks

Despite the greater number of blocks for deeper layers (2120 blocks) compared to the uppermost layer (530 blocks) of blocks, the identification of fewer archetypes in the deeper layers is not unexpected. This is due to the increased homogeneity in hydrogeological features and the absence of built structures at these depths. The upper temperature BC emerges as the most influential feature in determining archetype classification in deeper blocks (Figure 11b). Given the strong relationship between upper and lower temperature BCs and the volumetric temperature of deeper block models, these BCs dominate the decision-tree process, and the other features were not used by the regressor to split the data. Furthermore, due to the homogeneity of geological layers, features such as thermal conductivity, heat capacity, and porosity exhibit only a narrow range of values and are therefore not used to split the nodes.

3.4 Application of archetypes for geothermal management

To showcase an application of the archetype approach for subsurface management purposes (Figure 1, step 6), the 38 identified groundwater archetypes (Figure 10b) are assigned to specific groups of geothermal archetypes (A_{Geo}) by using simplified criteria of geothermal suitability for GSHP systems. Archetypes with predicted volumetric temperatures higher than 13°C, and an average thermal conductivity above 1.5 W/mK are categorized into 10 geothermal archetypes, from A_{Geo1} with the lowest temperature and thermal conductivity to A_{Geo10} with the highest temperature and thermal conductivity (Figure 12, Table A-1). Higher building densities leads to less available space for geothermal use in densely built-up areas (Tissen et al., 2021). Furthermore, installing geothermal systems in public spaces is not yet permitted in Berlin. Therefore, archetypes with more than 25% of surface area being occupied by built infrastructure are not included in the geothermal archetypes.

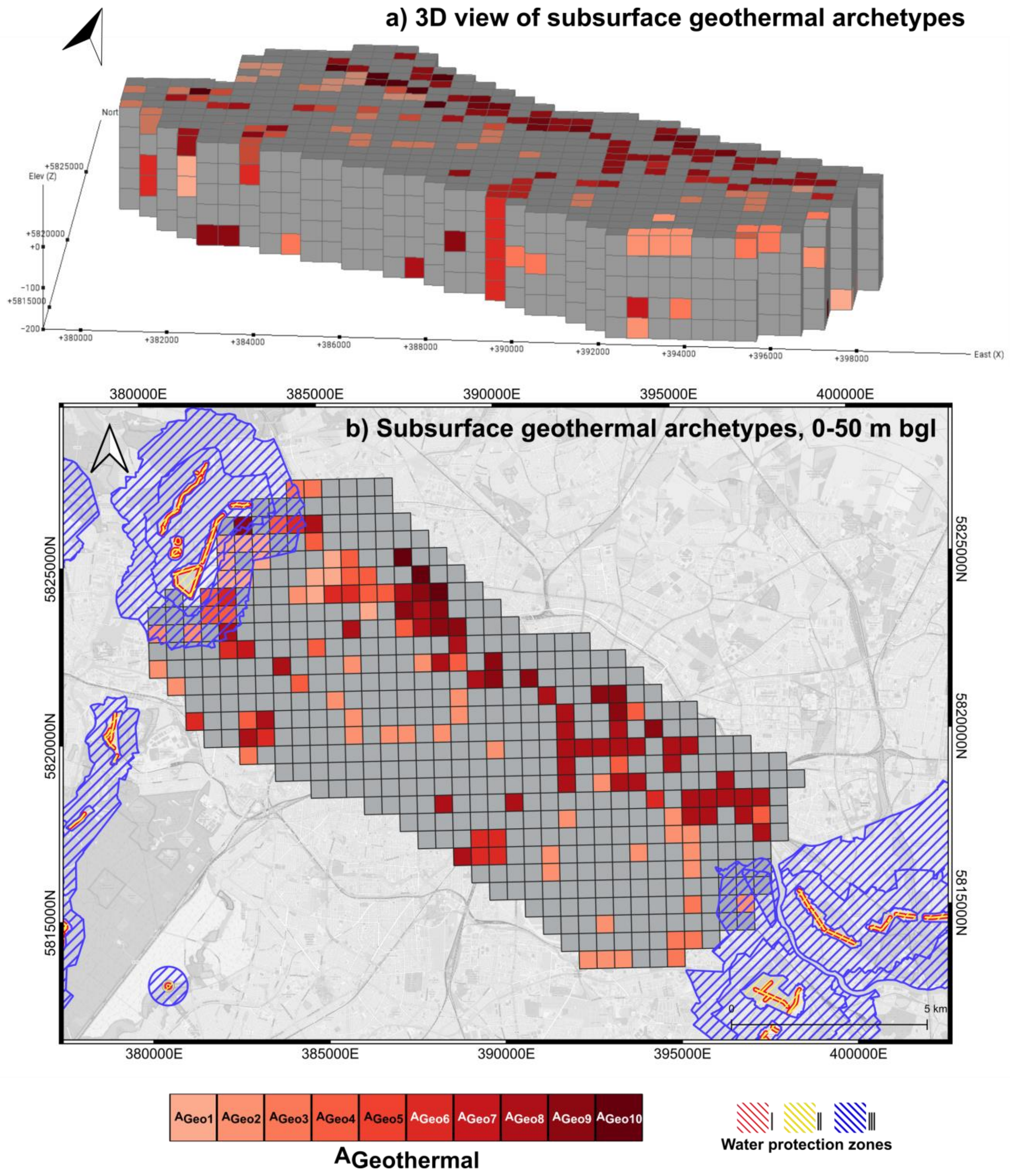

Figure 12: a) 3D view of geothermal archetypes, and b) classified geothermal archetypes (Figure 1, step 6). The locations of water protection zones are also included.

The geothermal archetypes highlight areas deemed particularly suitable for geothermal utilization. This information can be useful to local authorities or industries and contribute to driving investment and leading to a wider utilization of these sustainable technologies. The archetype approach can easily be combined and enhanced with additional information, such as water protection zones (WPZ) (Figure 12b), which play a key role for geothermal planning. Geothermal applications in water protection zones I (red) and II (yellow) are strictly prohibited. However, under certain conditions, installations could technically be allowed in zone III (blue) (Geoportal Berlin, 2024). The 3D archetype approach presented above can support management of such conflicting interests. For example, even if the uppermost block at a certain location may fall into a WPZ, one could discuss geothermal use for well-suited deeper blocks.

The identified archetypes can also support geothermal licensing processes by incorporating restrictions to e.g. shallow geothermal systems into the workflow. The 3D nature of the underlying block models allows integration and visualization of e.g. spatially varying limitations in drilling depth for BHE and wells. For example, in Berlin, the Rupelian clay must not be drilled into as it acts as a hydraulic barrier (Geoportal Berlin, 2024) between saline water and freshwater aquifers. Similarly, in the German state of Baden-Württemberg geological layers containing sulphate minerals impose depth limitations for geothermal drilling due to geotechnical risks of anhydrate swelling (Menberg et al., 2025). Also, regulatory restrictions, such as groundwater protection zones, can easily be integrated into the archetype framework by marking the blocks in the corresponding area, or by creating a specific archetype class for water protection zones. If the geological model was extended to deeper layers (e.g. 3-4 kilometers depth) that are of interest for deep geothermal system, the 3D archetype approach could also help manage concurrent use of different geothermal and groundwater resources in different geological layers.

The archetype approach could be further expanded to other groundwater or subsurface uses, such as groundwater ecosystem protection, by defining corresponding criteria and thus supporting sustainable subsurface management. Finally, the thermo-hydraulic block models from the archetypes can serve as a basis for more detailed and high-resolution geothermal simulations, for example, for planning of groundwater heat pumps (GWHP) or aquifer thermal energy storage

(ATES), by providing local BCs and accounting for existing infrastructure. Previous studies have demonstrated the value of combining 3D geological models with groundwater flow and heat transport models for geothermal applications. For example, in a deep basin scale model, a detailed physics-based model was developed to assess large-scale thermal regimes (Alcanié et al., 2021). Similarly, the detailed geological modelling was assessed to quantify geothermal potential on a kilometer scale using isothermal surfaces (Zhu et al., 2020). The current study is also a physics-based model, however, it aims to balance the physical processes' accuracy and computational efficiency using the archetypes. The current approach can be combined with the detailed models mentioned above to compensate for the loss of local-scale details missing in the archetypes approach.

3.5 Comparison to other approaches and limitations of the study

Previous studies have demonstrated the value of combining 3D geological models with groundwater flow and heat transport models for deep geothermal applications. For example, in a basin-scale study, a detailed physics-based model was developed to assess large-scale thermal regimes (Alcanié et al., 2021). This study showed that regional thermal regimes are primarily controlled by large-scale groundwater flow and boundary conditions, allowing suggestions for the location of deep geothermal wells. The role of groundwater flow and boundary conditions in the present study is consistent with the findings from Alcanié et al. (2021). While Alcanié et al. (2021) focused on deep, basin-scale processes, the present study highlights the importance of the anthropogenically influenced thermal regime in the shallow subsurface and its impact on shallow geothermal energy. Similarly, detailed geological models have previously been assessed to quantify geothermal potential on a kilometer scale using isothermal surfaces (Zhu et al., 2020). The study results are in line with the current study, which suggests that the favorable geothermal conditions are linked to specific geothermal and thermal configurations. In addition, the present study prioritizes spatial comparability, computational efficiency and the applicability to urban subsurface management.

In this context, the applicability of the proposed method is influenced by the availability and quality of subsurface data. This study demonstrates how high-quality data, such as the geospatial data for the Berlin area, can be utilized to quantify the thermal state of the subsurface and the potential for shallow geothermal energy. However, it is important to note that data on a comparable level of detail is not always available. Yet, for most urban areas on the globe basic information on geological and hydrogeological conditions, such as dominating surface geology (Hartmann and Moosdorf, 2012) and groundwater table depth, is available (Fan et al., 2012). The same is true for basic anthropogenic infrastructure, such as building footprints (Zhu et al., 2025), and land use (Zanaga et al., 2021), which will allow simplified (hydro)geological modelling and basic archetype identification. Also, the block size in the approach can be reduced or increased accordingly to reflect the quantity and quality of the spatial data used.

Beyond the current application to Berlin, the proposed approach also allows for integration of additional data sources and complementary modeling approaches. For example, geophysical data, such as electrical resistivity tomography or seismic exploration data, can be used to refine the geological model and thus improve model confidence. Moreover, as the FEFLOW software incorporates solute transport modelling, it is also possible to include chemical compounds in the archetypes identification and assess thermo-chemical interactions and their impact on groundwater quality at the city-scale. Likewise, the archetype-based approach could be expanded to investigate thermo-hydro-mechanical processes in order to evaluate city-scale subsurface deformations associated with thermal use of subsurface, using compatible software such as COMSOL.

4. Conclusions

In this study, a detailed 3D geological model as well as numerical groundwater flow and heat transport block models are used to derive a spatially resolved overview of the thermal state of the urban subsurface in Berlin, Germany. Groundwater archetypes for the study area are identified, and the impact of (hydro)geological and infrastructure features on archetypes identification is investigated. Moreover, building upon the identified groundwater archetypes, geothermal archetypes are defined to assess the suitability for GSHP systems.

There is a good spatial agreement between the large-scale patterns of simulated groundwater temperatures (GWT) and interpolated maps in the uppermost layer of the numerical block models, where the groundwater temperature is mostly affected by the anthropogenic factors such as building basements and UCPs. The block models are also able to predict GWT hot spots like Alexanderplatz (with the average GWT of 14.3°C for involved blocks) with several basements and train tunnels, and low GWT in large green areas like Tiergarten (with the average GWT of 12.1°C for involved blocks), which are not observed in measured interpolated maps. Some discrepancies (0.6°C) exist between the simulated and interpolated maps from measurements of all blocks. These may result from uncertainties in model inputs, such as basement temperature or hydrogeological parameters (e.g., thermal and hydraulic conductivities), as well as the spatial bias of measurement well locations and shortcomings of statistical interpolation.

Considering a balance between computational efficiency and accuracy, 38 archetypes for the near-surface layer of blocks and 21 archetypes for the deeper layers are identified using regression trees. The similarity of large-scale spatial GWT patterns obtained by defining varying numbers of archetypes (10, 17, 38, and 82) indicates robustness of the approach, regardless of the number of archetypes selected based on different tolerance values.

By combining simple criteria, such as thermal conductivity and GWT, 10 out of the 38 groundwater archetypes are classified as geothermal archetypes, indicating suitable areas for GSHP systems. The nature of the archetype approach based on the detailed parameterized block models also allows integration of further spatial and legal limitations, such as space taken up by urban infrastructure and water protection zones. Importantly, the differentiation of different depth layers of blocks with different feature importance offers opportunities for 3D subsurface management approaches, while the underlying numerical models of the archetypes can serve as a consistent basis for modelling and planning of different thermal or hydraulic groundwater uses. In the future, the archetypes approach could be developed further to support a broader range of groundwater and subsurface uses by considering, e.g., infrastructure in more detail or groundwater-dependent ecosystems.

The results presented in this work support the use of this flexible and scalable methodology for thermally quantifying the subsurface in a computationally efficient way and showcase how this approach can be adapted and combined with additional information to produce useful outputs. While the archetypes presented here are specific to Berlin, the methodological approach itself is universally transferable. Depending on the availability of geospatial data, the approach can be adapted to include other types of subsurface infrastructure, such as district heating networks, as well as surface structures, such as industrial sites, which impact the groundwater thermal regime and thus archetype identification. Also, the workflow can be easily applied in other geological settings, such as karst aquifers or crystalline bedrocks, by setting up a corresponding geological model and transferring it into a corresponding subsurface flow model suitable for the hydrogeological settings. The geothermal archetypes and maps can be adapted to include or prioritize different aspects of geothermal planning, such as heating demand to provide as much energy as possible or current heating accessibility to provide geothermal energy to those who most benefit from it. This can be done by matching heating supply with demand, for example, by incorporating demand data or by assessing the existing built infrastructure. These can lead to a wider utilization of the technology and therefore also contribute towards the pathway to net-zero.

Abbreviations

k_f	Hydraulic conductivity [m/s]
n_e	Effective porosity [-]
c_h	Heat capacity [MJ/m^{3}K]

$c_{h, unsat}$	Unsaturated heat capacity [MJ/m^{3}K]
λ	Thermal conductivity of solid [W/m K]
λ_{unsat}	Unsaturated thermal conductivity of solid [W/m K]
A_{Geo}	Geothermal archetypes
$A_{basements}$	Basement area percentage [%]
A_{ucp}	Underground car park area percentage [%]
$T_{upstream}$	Upstream temperature [°C]

Supplementary information

Table A-1: List of geothermal archetypes with their corresponding average volumetric temperature and thermal conductivity for uppermost layers of blocks (0-50m bgl).

Archetype	Volumetric temperature (°C)	Thermal conductivity (W/m.K)
A_{Geo1}	13.2	1.9
A_{Geo2}	13.3	1.6
A_{Geo3}	13.4	1.9
A_{Geo4}	13.5	1.7
A_{Geo5}	13.5	1.8
A_{Geo6}	13.6	1.8
A_{Geo7}	13.8	1.8
A_{Geo8}	13.9	1.6
A_{Geo9}	14.0	1.8
A_{Geo10}	14.2	2.0

Author contributions

K.M., M.J.K., N.M., and P.B. provided the topic and supervised the work. M.R.H. created the models, analyzed and interpreted the results. M.R.H. wrote the paper draft. K.M., M.J.K., N.M., and P.B. revised the paper.

Acknowledgments

The authors would like to thank Matthias Herrmann (KIT) for his valuable help during development of 3D geological model. We also highly appreciate the support from Jens Bölscher, Cathrin Dreher, and Marielle Geppert (Senate Department for Urban Mobility, transport, climate action, and environment of Berlin) for providing groundwater data.

Competing interests

The authors declare no competing interests.

Funding

This research has been supported by the Federal Ministry of Education and Research of Germany (BMBF) under the research project CHARMANT (FZK 02WGW1666A).

Data availability

The dataset used and/or analyzed during this work are available upon request from the corresponding author.

References

Alberto, P., & Crosta, G. B. (2021). Characterization of the subsurface urban heat island and its sources in the Milan city area, Italy. Hydrogeology Journal, 29(7), 2487-2500.

Alao, Joseph Omeiza, Kolawole Muideen Lawal, Bala Bello Muhammad Dewu, and Jimoh Raimi. "Detection of shallow underground targets using electrical resistivity tomography and the implications in civil/environmental engineering." Discover Geoscience 2, no. 1 (2024): 52.

Alcanié M, Collignon M, Møyner O, Lupi M. 3D Basin-Scale Groundwater Flow Modeling as a Tool for Geothermal Exploration: Application to the Geneva Basin, Switzerland-France. Geochemistry, Geophysics, Geosystems. 2021 May;22(5):e2020GC009505.

Assouline D, Mohajeri N, Gudmundsson A, Scartezzini JL. A machine learning approach for mapping the very shallow theoretical geothermal potential. Geothermal Energy. 2019 Jul 25;7(1):19.

Attard G, Rossier Y, Winiarski T, Eisenlohr L. Deterministic modeling of the impact of underground structures on urban groundwater temperature. Science of the Total Environment. 2016 Dec 1;572:986-94.

Bayer P, Attard G, Blum P, Menberg K. The geothermal potential of cities. Renewable and Sustainable Energy Reviews. 2019 May 1;106:17-30.

Barla M, Di Donna A, Baralis M. City-scale analysis of subsoil thermal conditions due to geothermal exploitation. Environmental Geotechnics. 2020 Jul 6;7(4):306-16.

Becher J, Englisch C, Griebler C, Bayer P. Groundwater fauna downtown–Drivers, impacts and implications for subsurface ecosystems in urban areas. Journal of Contaminant Hydrology. 2022 Jun 1;248:104021.

Benz SA, Bayer P, Menberg K, Jung S, Blum P. Spatial resolution of anthropogenic heat fluxes into urban aquifers. Science of the Total Environment. 2015 Aug 15;524:427-39.

Benz SA, Irvine DJ, Rau GC, Bayer P, Menberg K, Blum P, Jamieson RC, Griebler C, Kurylyk BL. Global groundwater warming due to climate change. Nature Geoscience. 2024 Jun;17(6):545-51.

Bidarmaghz A, Choudhary R, Soga K, Kessler H, Terrington RL, Thorpe S. Influence of geology and hydrogeology on heat rejection from residential basements in urban areas. Tunnelling and Underground Space Technology. 2019 Oct 1;92:103068.

Bidarmaghz A, Choudhary R, Soga K, Terrington RL, Kessler H, Thorpe S. Large-scale urban underground hydro-thermal modelling–A case study of the Royal Borough of Kensington and Chelsea, London. Science of the total environment. 2020 Jan 15;700:134955.

Blum P, Menberg K, Koch F, Benz SA, Tissen C, Hemmerle H, Bayer P. Is thermal use of groundwater a pollution?. Journal of Contaminant Hydrology. 2021 May 1;239:103791.

Böttcher F, Zosseder K. Thermal influences on groundwater in urban environments–A multivariate statistical analysis of the subsurface heat island effect in Munich. Science of The Total Environment. 2022 Mar 1;810:152193.

Brielmann H, Lueders T, Schreglmann K, Ferraro F, Avramov M, Hammerl V, Blum P, Bayer P, Griebler C. Oberflächennahe Geothermie und ihre potenziellen Auswirkungen auf Grundwasserökosysteme. Grundwasser. 2011 Jun;16(2):77-91.

Ciampi P, Felli G, Feriaud D, Esposito C, Petrangeli Papini M. 3D GeoRemediation: A Digital Hydrogeophysical–Chemical Clone and Virtual Hydraulic Barrier with Groundwater Circulation Wells (GCWs) for Groundwater Remediation. Sustainability. 2024 Jun 19;16(12):5216.

Čypaitė V, Herms I, Arnó G, Nuñez JA, Colomer M, Camps V, Baxter C. 3D Conceptual Model Approach for the Assessment of Shallow Geothermal Potential in Urban Areas: The Case Study of the Girona city (preliminary results). InProceedings World Geothermal Congress 2020 (p. 1).

Deutscher Wetterdienst (DWD),). Web-based weather request and distributionsystemhttp://www.dwd.de/

Diersch HJ. FEFLOW: finite element modeling of flow, mass and heat transport in porous and fractured media. Springer Science & Business Media; 2013 Nov 22.

Epting J, Huggenberger P. Unraveling the heat island effect observed in urban groundwater bodies–Definition of a potential natural state. Journal of hydrology. 2013 Sep 25;501:193-204.

Epting J, Händel F, Huggenberger P. Thermal management of an unconsolidated shallow urban groundwater body. Hydrology and Earth System Sciences. 2013 May 15;17(5):1851-69.

Epting J, Böttcher F, Mueller MH, García-Gil A, Zosseder K, Huggenberger P. City-scale solutions for the energy use of shallow urban subsurface resources–Bridging the gap between theoretical and technical potentials. Renewable Energy. 2020 Mar 1;147:751-63.

Eskilson, P. (1987). Thermal analysis of heat extraction boreholes (PhD), University of Lund, Lund, 1987

Fan Y, Li H, Miguez-Macho G. Global patterns of groundwater table depth. Science. 2013 Feb 22;339(6122):940-3.

Ferguson G, Woodbury AD. Urban heat island in the subsurface. Geophysical research letters. 2007 Dec 16;34(23).

Frick M, Scheck-Wenderoth M, Schneider M, Cacace M. Surface to groundwater interactions beneath the city of Berlin: results from 3D models. Geofluids. 2019;2019(1):4129016.

García-Gil A, Vázquez-Suñe E, Schneider EG, Sánchez-Navarro JÁ, Mateo-Lázaro J. The thermal consequences of river-level variations in an urban groundwater body highly affected by groundwater heat pumps. Science of the total Environment. 2014 Jul 1;485:575-87.

García-Gil, A., Vázquez-Suñe, E., Alcaraz, M. M., Juan, A. S., Sánchez-Navarro, J. Á., Montlleó, M., ... & Lao, J. (2015). GIS-supported mapping of low-temperature geothermal potential taking groundwater flow into account. *Renewable energy*, *77*, 268-278.

Geoportal Berlin, 2024. Senatsverwaltung für Stadtentwicklung, Bauen und Wohnen.URL. https://fbinter.stadt-berlin.de/fb/index.jsp.

GÖTHEL M, HERMSDORF N. Überblick zur regionalgeologischen Situation im Land Brandenburg einschließlich Berlin.Hastie, T. (2009). The elements of statistical learning: data mining, inference, and prediction.

Hartmann J, Moosdorf N. The new global lithological map database GLiM: A representation of rock properties at the Earth surface. Geochemistry, Geophysics, Geosystems. 2012 Dec;13(12).

Hoffmann C, Geissler A. The prebound-effect in detail: real indoor temperatures in basements and measured versus calculated U-values. Energy Procedia. 2017 Sep 1;122:32-7.

Hölting B, Coldewey WG. Hydrogeologie: Einführung in die allgemeine und angewandte Hydrogeologie. Springer-Verlag; 2019 Oct 20.

Hemmerle H, Ferguson G, Blum P, Bayer P. The evolution of the geothermal potential of a subsurface urban heat island. Environmental Research Letters. 2022 Jul 25;17(8):084018.

nnoSÜD. (n.d.). Geothermie Software. Retrieved March 25, 2025, from https://innosued.de/energie/geothermie-software-2/

Issartel J, Hervant F, Voituron Y, Renault D, Vernon P. Behavioural, ventilatory and respiratory responses of epigean and hypogean crustaceans to different temperatures. Comparative Biochemistry and Physiology Part A: Molecular & Integrative Physiology. 2005 May 1;141(1):1-7.

Kalogirou SA, Florides GA, Pouloupatis PD, Panayides I, Joseph-Stylianou J, Zomeni Z. Artificial neural networks for the generation of geothermal maps of ground temperature at various depths by considering land configuration. Energy. 2012 Dec 1;48(1):233-40.

Kho JC, Loke WS, Wong ZZ, Raghunandan ME. Impact of rising temperatures on urban underground infrastructure: A state-of-the-art review. Tunnelling and Underground Space Technology. 2025 Oct 1;164:106835.

Kreitmair MJ, Makasis N, Bidarmaghz A, Terrington RL, Farr GJ, Scheidegger JM, Choudhary R. Effect of anthropogenic heat sources in the shallow subsurface at city-scale. InE3S Web of Conferences 2020 (Vol. 205, p. 07002). EDP Sciences.

Kreitmair MJ, Makasis N, Bidarmaghz A, Menberg K, Choudhary R, Soga K. Finding common ground: A methodology for city-scale subsurface thermal modelling. Urban Climate. 2023 May 1;49:101513.

Koch F, Menberg K, Schweikert S, Spengler C, Hahn HJ, Blum P. Groundwater fauna in an urban area: natural or affected?. Hydrology and Earth System Sciences Discussions. 2020 May 6;2020:1-23.

Koch F, Blum P, Korbel K, Menberg K. Global overview on groundwater fauna. Ecohydrology. 2024 Jan;17(1):e2607.

Koch, F (2024). Spatial and temporal analysis of groundwater ecosystems. Dissertation 2024, Mai 29. Karlsruher Institut für Technologie (KIT). doi:10.5445/IR/1000170889

Limberg AL, Thierbach JE. Gliederung der Grundwasserleiter in Berlin. Brandenburgische Geowissenschaftliche Beiträge. 1997;4(2):21-6.

Limberg A, Thierbach J. Hydrostratigrafie von Berlin-Korrelation mit dem Norddeutschen Gliederungsschema. Brandenburgische Geowissenschaftliche Beiträge. 2002;9(1/2):65-8.

Loria AF, Thota A, Thomas AM, Friedle N, Lautenberg JM, Song EC. Subsurface heat island across the Chicago Loop district: Analysis of localized drivers. Urban Climate. 2022 Jul 1;44:101211.

Makasis N, Kreitmair MJ, Bidarmaghz A, Farr GJ, Scheidegger JM, Choudhary R. Impact of simplifications on numerical modelling of the shallow subsurface at city-scale and implications for shallow geothermal potential. Science of the Total Environment. 2021 Oct 15;791:148236.

Menberg K, Bayer P, Zosseder K, Rumohr S, Blum P. Subsurface urban heat islands in German cities. Science of the total environment. 2013 Jan 1;442:123-33.

Menberg K, Blum P, Schaffitel A, Bayer P. Long-term evolution of anthropogenic heat fluxes into a subsurface urban heat island. Environmental science & technology. 2013 Sep 3;47(17):9747-55.

Menberg K, Bidarmaghz A, Gregory A, Choudhary R, Girolami M. Multi-fidelity approach to Bayesian parameter estimation in subsurface heat and fluid transport models. Science of the Total Environment. 2020 Nov 25;745:140846.

Menberg K, Hemmerle H, Bayer P, Bott C, Bidarmaghz A, Ferguson G, Bloemendal M, Blum P. Opportunities, benefits and impacts of shallow geothermal energy. Nature Reviews Earth & Environment. 2025 Nov 18:1-6.

Mueller MH, Huggenberger P, Epting J. Combining monitoring and modelling tools as a basis for city-scale concepts for a sustainable thermal management of urban groundwater resources. Science of the Total Environment. 2018 Jun 15;627:1121-36.

Ngarambe J, Raj S, Yun GY. Subsurface urban heat islands: From prevalence and drivers to implications for geothermal energy and a proposed new framework based on machine learning. Sustainable Cities and Society. 2025 Jan 18:106153.

Noethen M, Hemmerle H, Menberg K, Epting J, Benz SA, Blum P, Bayer P. Thermal impact of underground car parks on urban groundwater. Science of the Total Environment. 2023 Dec 10;903:166572.

Noethen M, Becher J, Menberg K, Blum P, Schüppler S, Metzler E, Rasch G, Griebler C, Bayer P. Environmental impact of an anthropogenic groundwater temperature hotspot. Science of The Total Environment. 2024 Dec 10;955:177153.

Ohmer M, Klester A, Kissinger A, Mirbach S, Class H, Schneider M, Lindenlaub M, Bauer M, Liesch T, Menberg K, Blum P. Berechnung von Temperaturfahnen im Grundwasser mit analytischen und numerischen Modellen. Grundwasser. 2022 Jun;27(2):113-29.

Previati A, Epting J, Crosta GB. The subsurface urban heat island in Milan (Italy)-A modeling approach covering present and future thermal effects on groundwater regimes. Science of the Total Environment. 2022 Mar 1;810:152119.

Pelzer J, Verburg C, Heinlein A, Schulte M. Few-Shot Learning by Explicit Physics Integration: An Application to Groundwater Heat Transport. arXiv preprint arXiv:2507.06062. 2025 Jul 8.

Pophillat W, Attard G, Bayer P, Hecht-Méndez J, Blum P. Analytical solutions for predicting thermal plumes of groundwater heat pump systems. Renewable Energy. 2020 Mar 1;147:2696-707.

Radioti G, Sartor K, Charlier R, Dewallef P, Nguyen F. Effect of undisturbed ground temperature on the design of closed-loop geothermal systems: A case study in a semi-urban environment. Applied energy. 2017 Aug 15;200:89-105.

Rock G, Kupfersberger H. 3D modeling of groundwater heat transport in the shallow Westliches Leibnitzer Feld aquifer, Austria. Journal of Hydrology. 2018 Feb 1;557:668-78.

OpenStreetMap contributors, 2017. Data mining using the Overpass API in QGIS,https://www.openstreetmap.org.

Sartirana D, Rotiroti M, Zanotti C, Bonomi T, Fumagalli L, De Amicis M. A 3D geodatabase for urban underground infrastructures: implementation and application to groundwater management in Milan metropolitan area. ISPRS International Journal of Geo-Information. 2020 Oct 21;9(10):609.

Seequent, 2024. Leapfrog Geo. Seequent. Bentley Systems, Incorporated. https://www.seequent.com/products-solutions/leapfrog-geo.

Sippel J, Fuchs S, Cacace M, Braatz A, Kastner O, Huenges E, Scheck-Wenderoth M. Deep 3D thermal modelling for the city of Berlin (Germany). Environmental Earth Sciences. 2013 Dec;70(8):3545-66.

Stemmle R, Lee H, Blum P, Menberg K. City-scale heating and cooling with aquifer thermal energy storage (ATES). Geothermal energy. 2024 Jan 18;12(1):2.

Sun T, Luo Z, Chay T. An analytical model to predict the temperature in subway-tunnels by coupling thermal mass and ventilation. Journal of Building Engineering. 2021 Dec 1;44:102564.

Verein Deutscher Ingenieure (VDI). (2010). *VDI 4640 Part 1: Thermal use of the underground – Fundamentals, approvals, environmental aspects*. Düsseldorf, Germany.

Taniguchi M, Shimada J, Fukuda Y, Yamano M, Onodera SI, Kaneko S, Yoshikoshi A. Anthropogenic effects on the subsurface thermal and groundwater environments in Osaka, Japan and Bangkok, Thailand. Science of the total environment. 2009 Apr 15;407(9):3153-64.

Tissen C, Menberg K, Benz SA, Bayer P, Steiner C, Götzl G, Blum P. Identifying key locations for shallow geothermal use in Vienna. Renewable Energy. 2021 Apr 1;167:1-9.

Wu Q, Xu H, Zou X. An effective method for 3D geological modeling with multi-source data integration. Computers & geosciences. 2005 Feb 1;31(1):35-43.

Zanaga, D., Van De Kerchove, R., De Keersmaecker, W., et al. (2021). ESA WorldCover 10 m 2020 global land cover map. European Space Agency. https://doi.org/10.5281/zenodo.5571936

Zhu K, Bayer P, Grathwohl P, Blum P. Groundwater temperature evolution in the subsurface urban heat island of Cologne, Germany. Hydrological processes. 2015 Mar 15;29(6):965-78.

Zhu K, Blum P, Ferguson G, Balke KD, Bayer P. The geothermal potential of urban heat islands. Environmental Research Letters. 2010 Oct 12;5(4):044002.

Zhu XX, Chen S, Zhang F, Shi Y, Wang Y. GlobalBuildingAtlas: an open global and complete dataset of building polygons, heights and LoD1 3D models. Earth System Science Data Discussions. 2025 Jul 8;2025:1-31.

Zhu Z, Lei X, Xu N, Shao D, Jiang X, Wu X. Integration of 3D geological modeling and geothermal field analysis for the evaluation of geothermal reserves in the northwest of Beijing Plain, China. Water. 2020 Feb 27;12(3):638.